

Sandia National Laboratories, California  
Thin-Film & Interface Research Program

*Highlights 1999*

**Science of Metals**

Dislocation Structures near the Commensurate-Incommensurate Phase Transition:	
Ag on Pt(111).....	2
Compact Cluster Surface Diffusion by Concerted Rotation and Translation.....	4
Multi-Scale Modeling of Grain Boundary De-faceting Phase Transition.....	6
Direct Gap in Ordered Silicon Carbon Alloys.....	8
Electron Energy Loss in Transition-Metal Carbides.....	10
Mn doping in GaAs.....	12
Generalizations of Peierls-Nabarro Model.....	14
Electronic Structure Methods Development.....	16
Probing the mechanisms for self-assembly on metal surfaces: thermal fluctuations of the Au(111) herringbone reconstruction.....	18
Strain Effects on diffusion in FCC Metals.....	20
Predicting strength from microstructure.....	22
Stacking Fault Energy and Microstructure Effects on Torsion Texture Evolution.....	24
Short-range Order in Dislocation Boundary Structures.....	26
Factorization of Correlations in Dislocation Structures.....	28
Dislocation-Based Model for the FCC to 9R Reconstruction at a $90^\circ\{111\}/\{211\}$ Boundary in Gold.....	30
Determination of the Surface Structure of $\alpha\text{-Al}_2\text{O}_3$ (0001).....	32

**Alloy Theory**

Alloy Theory: Non-Configurational Entropies in Metallic Alloys.....	34
Surface Alloys.....	36

**Advanced Ceramics**

Computation of the Solid-Liquid Interfacial Free Energy in Ni.....	38
--	----

**Dislocation Structures near the Commensurate-Incommensurate Phase Transition:  
Ag on Pt(111)  
J. C. Hamilton**

**Motivation:**

Submonolayer films of Ag on Pt(111) exhibit parallel partial dislocations separated by narrow hcp domains and much wider fcc domains. The large difference in width of the two domains is atypical of strained metal overlayers on close-packed substrates. However, similar domain widths have been observed for the clean Pt(111) reconstructed surface near the transition temperature from a bulk terminated to a dislocated surface. The origin of these domain widths remained obscure until the present work. Experiments also show an interesting island size dependence of dislocation structures which we can explain using the same 2D Frenkel Kontorova (FK) model used to understand the relative hcp and fcc domain widths.

**Accomplishment:**

We used a 2D FK model to simulate the experimental results. The substrate potential was derived from first-principles calculations. The adatom-adatom potential was a Morse potential. Initially the Morse potential parameters were chosen to match bulk Ag properties. By adjusting the Morse potential slightly we were able to reproduce the experimental domain widths. The domain widths were extremely sensitive to the Morse potential parameters because the system was very near to the commensurate-incommensurate transition. Approaching this transition from the incommensurate side, the spacing of dislocation pairs (ie the fcc domain width) increases rapidly diverging to infinity at the transition point. Once a suitable Morse potential had been determined, this potential was used to study the structure of dislocations in islands as a function of island size. Figure 1 shows four different structures considered for a 266Å wide island. All of these structures have been observed experimentally. Figure 2 shows the relative energy of the dislocation configurations as a function of island size.

**Significance:**

We have modeled the structure of dislocations both in submonolayer films and in islands of Ag on Pt(111). This model provides a simple understanding of the relative fcc and hcp domain widths for this system and also for the clean Pt(111) reconstruction. We have also applied this model to dislocation structures of nearly hexagonal islands as a function of island size. The model is able to predict the fact that pseudomorphic islands persist as sizes much greater than the dislocation spacing for a submonolayer film. We show that the equilibrium island shape is nearly hexagonal, with or without dislocations in the Ag island.

**Publications:**

"Dislocation Structures of Sub-Monolayer Films Near the Commensurate-Incommensurate Phase Transition: Ag on Pt(111)", J.C. Hamilton, R. Stumpf, Karsten Bromann, Marcella Giovannini, Klaus Kern, Harald Brune, Phys. Rev. Lett. **82**, 4488 (1999).

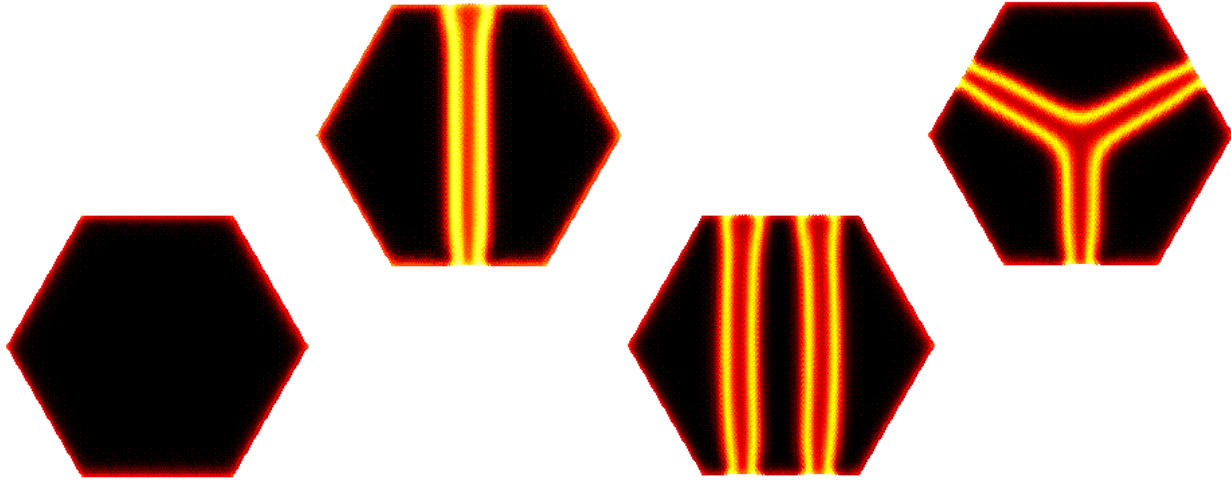


FIGURE 1: Possible dislocation structures for hexagonal islands of Ag on Pt(111). At the lower left is a dislocation free island. Next is an island with a pair of partial dislocations bounding a narrow region of hcp Ag. After that is an island with two pairs of partial partial dislocations. At the upper right is a "Y" dislocation pattern.

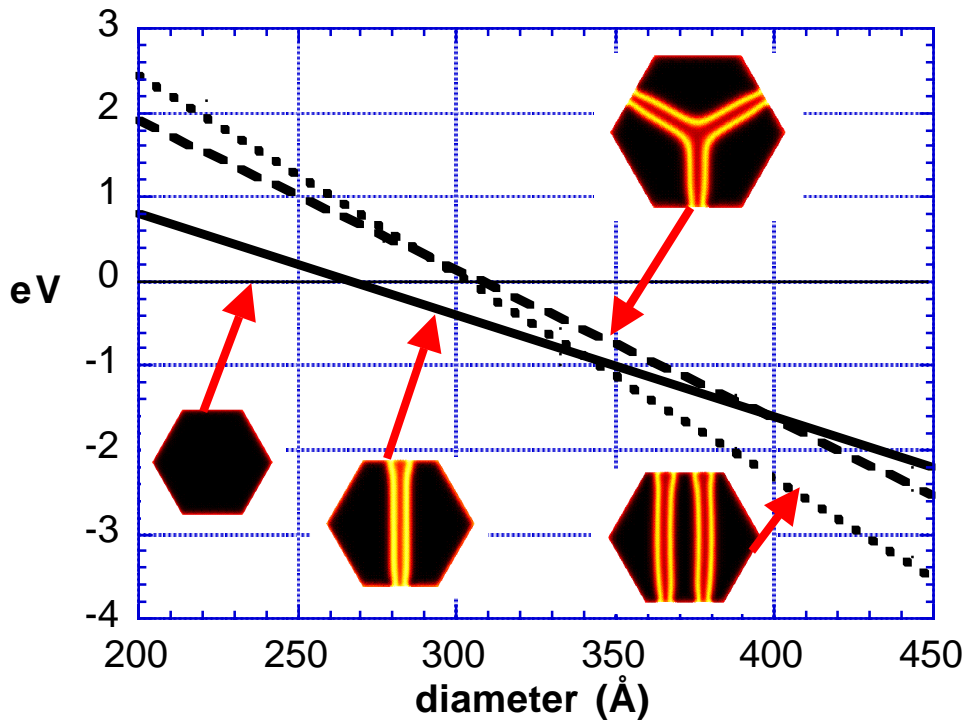


FIGURE 2: Calculated hexagonal island energies for various dislocation structures as a function of island size. All energies are referenced to the energy of a pseudomorphic island. For widths less than about  $240\text{\AA}$ , the pseudomorphic configuration is stable. For widths between  $240\text{\AA}$  and  $320\text{\AA}$ , the single dislocation pair configuration is stable. For widths greater than  $320\text{\AA}$ , the double dislocation pair is stable.

# Compact Cluster Surface Diffusion by Concerted Rotation and Translation

J. C. Hamilton and Arthur F. Voter

## Motivation:

Field ion microscopy experiments have shown that 7 and 19 atom Ir clusters on Ir(111) have remarkably high prefactors for diffusion, more than  $10^3$  times greater than for single atom diffusion. We have used first principles calculations to understand this dramatic effect. We discovered that a monolayer of Ir on Ir(111) has an unexpected metastable configuration with the monolayer atoms directly on top of the second atom layers. This discovery leads to the suggestion that compact Ir clusters may glide over the surface with atoms passing over the on-top sites. We have discovered a new mechanism, cartwheel-shuffle, which explains many of the experimental observations.

## Accomplishment:

A compact island of Ir on Ir(111) is similar to a pseudomorphic layer of Ir on Ir(111). In order to gain insight into the energetics of glide for a compact island, we first investigated the energies required to translate a pseudomorphic layer of Ir at various positions on an Ir(111) surface. The resulting energy plot is shown in figure 1b and contrasted with the energy plot for a single atom as a function of position shown in figure 1a. This figure emphasizes the dramatic difference between moving a single atom across a surface and moving a pseudomorphic overlayer over a surface. For a single atom, diffusion will occur from an fcc site to an hcp site and then to an fcc site. For a monolayer of iridium atoms (as in a pseudomorphic island), one can imagine other paths, including simultaneous rotation and translation. Using nudged elastic band first principles calculations, we found two favorable paths for diffusion of a 19-atom iridium cluster, shown in figure 2. The first, bridge glide, has been proposed before. The second, cartwheel-shuffle, is totally new. Since the center of mass of the cluster passes over the on-top site with this mechanism, it can easily explain experimentally observed long-jumps.

## Significance:

Our calculations of activation energies and prefactors suggest that clusters can diffuse on the Ir surface by combined translation and rotation. This provides an explanation for the high prefactors and long jumps observed in field ion microscopy experiments. The discovery of a metastable on-top configuration for a pseudomorphic Ir monolayer on Ir(111) is a totally new idea since generally on-top sites are expected to be highly unstable.

## Publications:

Compact Surface-cluster Diffusion by Concerted Rotation and Translation, J. C. Hamilton, Mads R. Sorenson and Arthur F. Voter, Phys. Rev. B. **61**, (2000).

Failure of 1-D Models for Ir Island Diffusion on Ir(111), J. C. Hamilton and Arthur F. Voter, submitted to Phys. Rev. Lett.

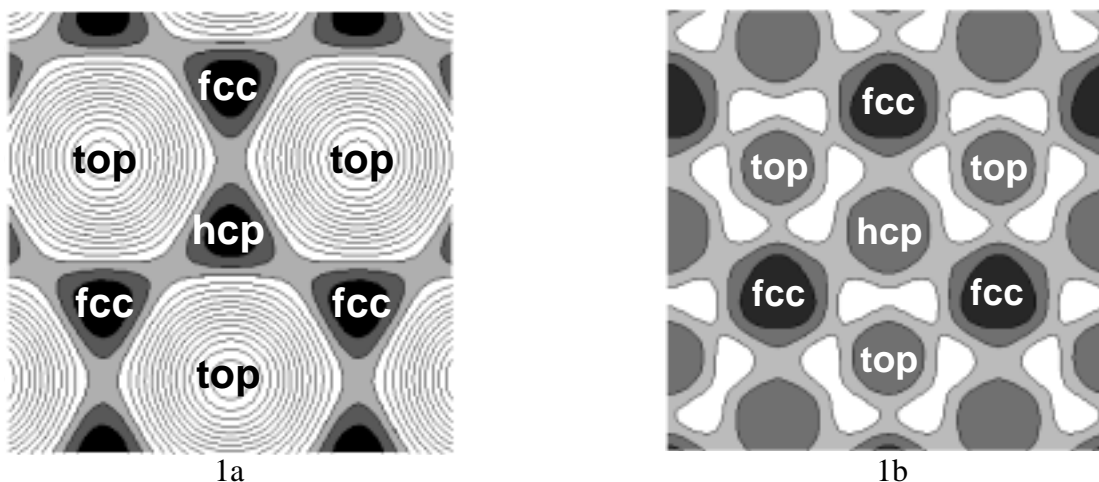


FIGURE 1: Relative energy per atom as a function of position for a single Ir atom on Ir(111) (fig 1a), and for a pseudomorphic Ir monolayer on Ir(111) (fig 1b). This figure demonstrates the dramatic difference between diffusing a single Ir atom on Ir(111) and shearing an Ir monolayer across Ir(111). For example the top site is unstable for an adatom and metastable for a monolayer. Contour intervals are 100 meV/atom in both plots. The gray scale is chosen to emphasize the portions of the energy surface most likely to be visited during diffusion.

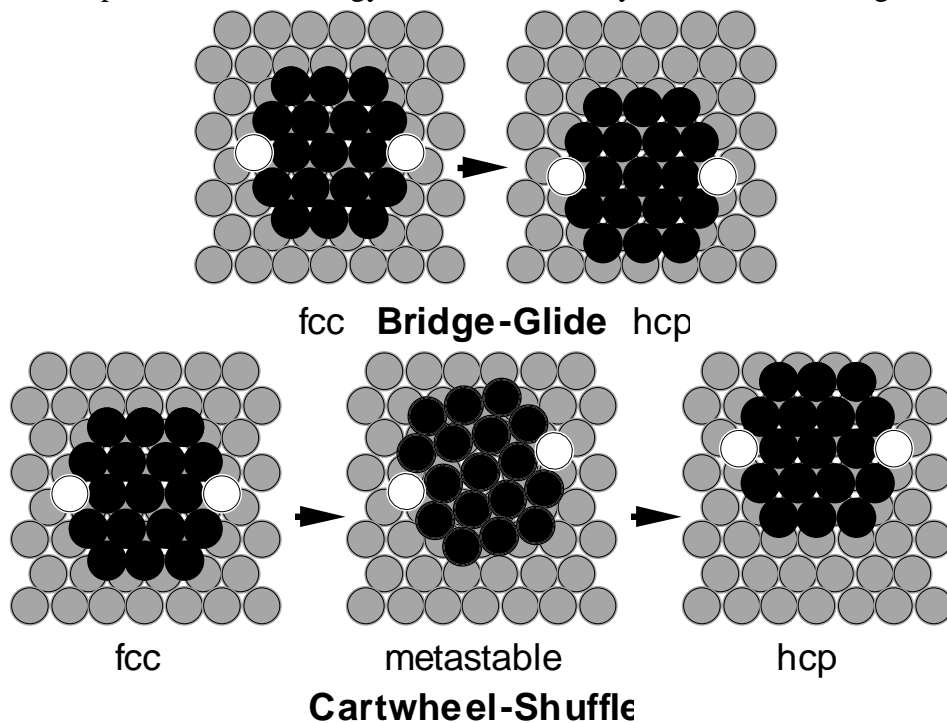


FIGURE 2: Two possible cluster glide mechanisms. Bridge-glide involves simultaneous translation of all cluster atoms over the bridge sites. Cartwheel-shuffle involves translation of the center atom to the on-top site while the cluster rotates by  $\sim 15^\circ$  to form a metastable state. The cluster then translates to another hollow site while rotating back by  $\sim 15^\circ$ .

# Multi-Scale Modeling of Grain Boundary De-faceting Phase Transition

J.C Hamilton and I. Daruka

## Motivation:

Thermodynamic studies have predicted that phase transitions should occur at grain boundaries in solids. These predictions have been confirmed by hot-stage transmission electron microscope studies revealing a reversible de-faceting transition of  $\Sigma 3\{112\}$  grain boundaries in Al at about 400K. In spite of its great practical and theoretical importance, the fundamental atomic processes involved in the de-faceting transition and the nature of the transition have not been resolved yet.

## Accomplishment:

We have carried out EAM molecular dynamics (MD) simulations of the  $\Sigma 3\{112\}$  grain boundaries in Al, using Voter-Chen aluminum potentials. At temperatures above 200K increasing disorder at the grain boundary facet junctions was observed with the grain boundary becoming smooth and diffuse at temperatures around and above 400K. This transition was reversible, the grain boundaries became faceted again upon cooling. We learned from these simulations that the grain boundary could move only by the collective motion of four atoms at the grain boundary junction (see insets of Fig. 1). This elementary excitation was mapped onto a simple two-dimensional lattice model incorporating both the geometry and the energy relations of the grain boundary. Extensive Monte-Carlo simulations were performed to investigate properties of the derived lattice model. In excellent agreement with the experiment and with the MD simulations, we found that at low temperatures the interface separating the two grains consists of faceted grain boundaries (Fig. 1a), while at high enough temperatures the facets disappear and the interface becomes rough at atomic length-scales (Fig. 1b). We showed that this de-faceting transition is a first-order phase transition in dramatic contrast to the continuous nature of surface roughening. Using the transfer-matrix method we were able to determine the phase transition temperature analytically.

## Significance:

Our results, derived with the help of multi-scale modeling, provide a detailed understanding of the experimentally observed de-faceting phase transition of grain boundaries. The formulated lattice model also enables us to study other related phenomena, such as grain coarsening, and grain mobility in other thin film systems. The nature of the elementary excitation and the discontinuity of the de-faceting phase transition emphasize the difference between our model and other discrete models aimed to describe grain boundary melting or surface roughening.

## Publications:

Grain Boundary Phase Transitions, J. C. Hamilton and I. Daruka, in preparation for submission to *Nature* magazine.

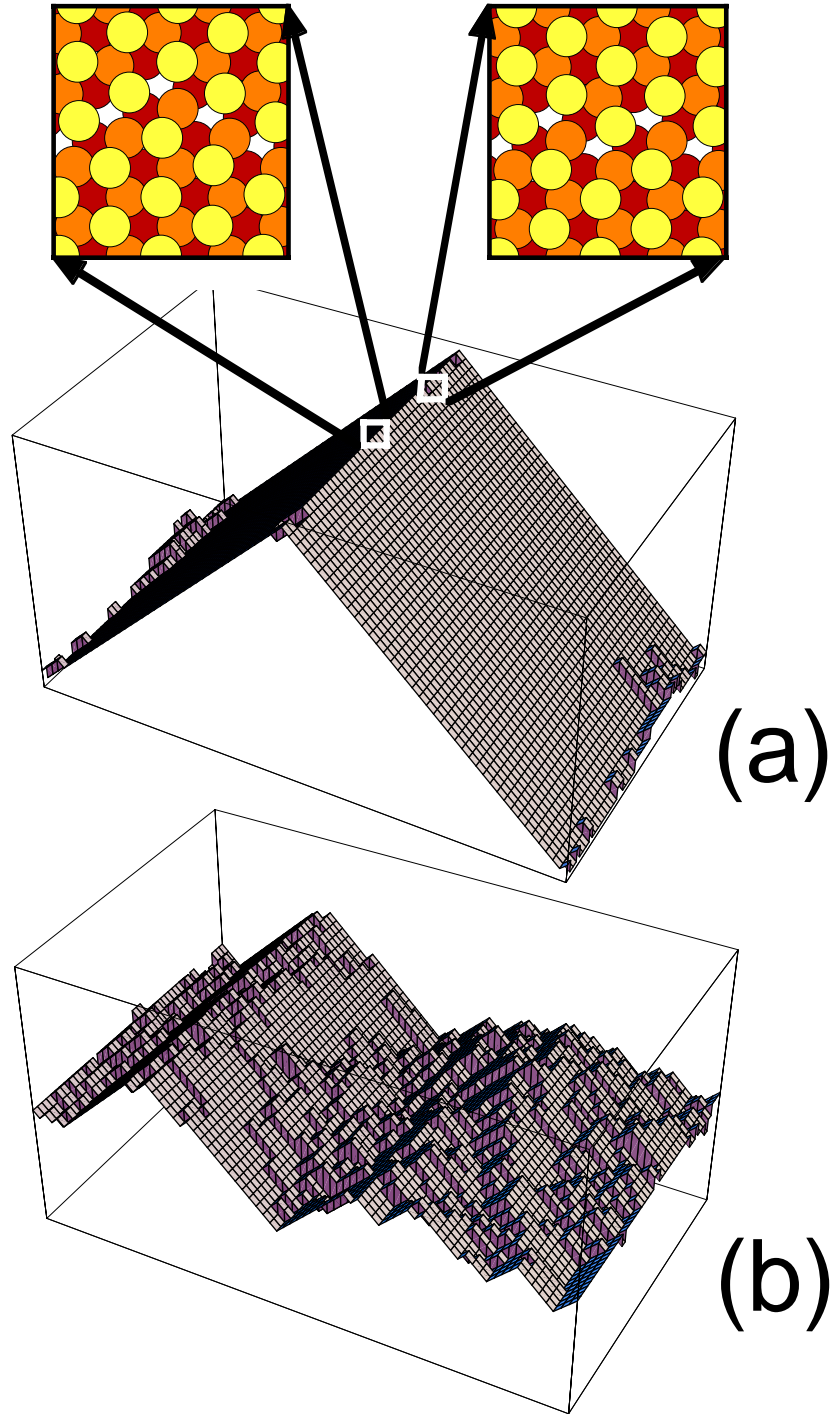


Fig. 1: Morphology of the  $\Sigma 3\{112\}$  grain boundaries in Al: (a) well below the de-faceting transition temperature, (b) around the de-faceting temperature, obtained by MC simulations. The left inset shows the atomic structure at the junction of the two  $\{112\}$  grain boundary facets viewed along  $[111]$ , calculated by embedded atom method simulations. The local rearrangement of atoms due to an elementary excitation at the junction is shown in the right inset.

## Direct Gap in Ordered Silicon Carbon Alloys

M. van Schilfgaarde

### Motivation:

Si has as one of its fundamental materials properties an indirect bandgap, which strongly limits its optical absorption. However, attempts to produce alloys of Si with other materials to make direct gaps have proved to be disappointing. Several studies predicted direct gap in SiGe superlattices. A direct gap was observed in strained, short-period SiGe superlattices and was explained in terms of zone folding in superlattice direction. However, the optical coupling of the valence band maximum (VBM) to the conduction band minimum (CBM) was found to be weak. Thus, no satisfactory direct-gap Si-based alloy has been found.

### Accomplishment:

We showed that alloying silicon with a few percent of carbon can render the bandgap direct with strong optical absorption, provided the carbon atoms are ordered. Addition of carbon introduces a significant s-character into the conduction band minimum, resulting in a large dipole matrix element. Explicit first-principles calculations of the optical absorption in ordered  $C_x Si_{1-x}$  alloys for  $x = 1/54$  and  $1/32$  show a near band edge absorption coefficient about half that of GaAs.

### Significance:

With silicon as the workhorse of the semiconductor industry, the possibility of obtaining direct gap in silicon has enormous technological importance for applications such as silicon-based lasers and optical computing. This work proposes one such way to realize this important but elusive goal.

### Publications:

S. Krishnamurthy, M. A. Berding, A. Sher, Mark van Schilfgaarde, and A.-B. Chen "Direct gap in ordered silicon carbon alloy," Appl. Phys. Lett. 75, 3153 (1999).

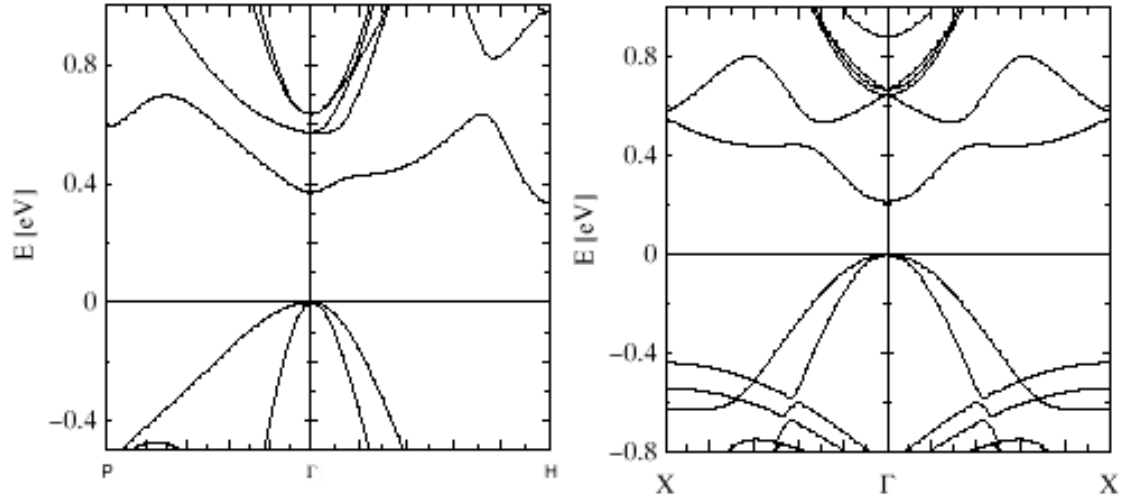


Fig. 1: (a) Energy bands of  $\text{CSi}_{31}$  in the body-centered-cubic arrangement. (b) Energy bands of  $\text{CSi}_{53}$  in the face-centered-cubic arrangement.

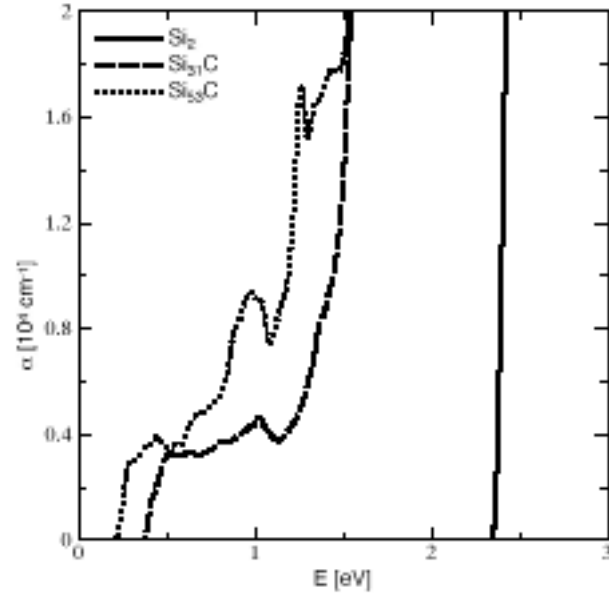


Fig. 2: Absorption coefficients of these compounds compared to Si.

## **Electron Energy Loss in Transition-Metal Carbides**

M. van Schilfgaarde

### **Motivation:**

The near edge and extended fine structure in electron energy loss spectroscopy (EELS) and X-ray absorption spectroscopy (XAS) contain a wealth of information about the electronic and atomic structure of solids. The absorption edge occurs when the beam has enough energy to excite a particular atomic core electron into the lowest unoccupied state, which in a metal is at the Fermi energy; thus EELS is an excellent technique to experimentally measure a quantity closely related to the local density-of-states.

### **Accomplishment:**

Our intention in the cited paper is to explore ways of explicitly calculating the near edge structure in EELS and XAS from first principles. While this has been done in the past by many authors, our approach calculates directly the EELS spectra from the relevant optical matrix element, rather than assuming a connection between the EELS spectra and the density of states.

We show that by using transition-state theory the accuracy of the threshold energy so that we can predict the energy loss in absolute terms. Second, we compare between explicit calculation of the dipole matrix element with the intuitively simpler task of evaluating the local density of states projected onto a suitable local orbital.

Finally we describe our discovery of how magnetism in CrN affects the measured spectrum and we propose a novel application of EELS and XANES, namely to probe the magnetic structure of alloys and its temperature dependence.

### **Significance:**

Comparing EELS spectra in pure materials to those with defects, information about the defect's environment can be deduced. Thus, EELS is an important experimental tool to for learning about the local environment of a defect. For interpretation of the data, a reliable theory of EELS is needed. This paper shows that a first-principles theory of the TM carbides agrees rather well with experimental data. The case of CrN offers an important example of how experiment and theory combined can provide insight into the magnetic ordering.

### **Publications:**

A. T. Paxton, M. van Schilfgaarde, M. MacKenzie and A. J. Craven, "The near-edge structure in energy-loss spectroscopy: many-electron and magnetic effects in transition metal nitrides and carbides," J. Phys. Cond. Matt. 12, 729 (2000).

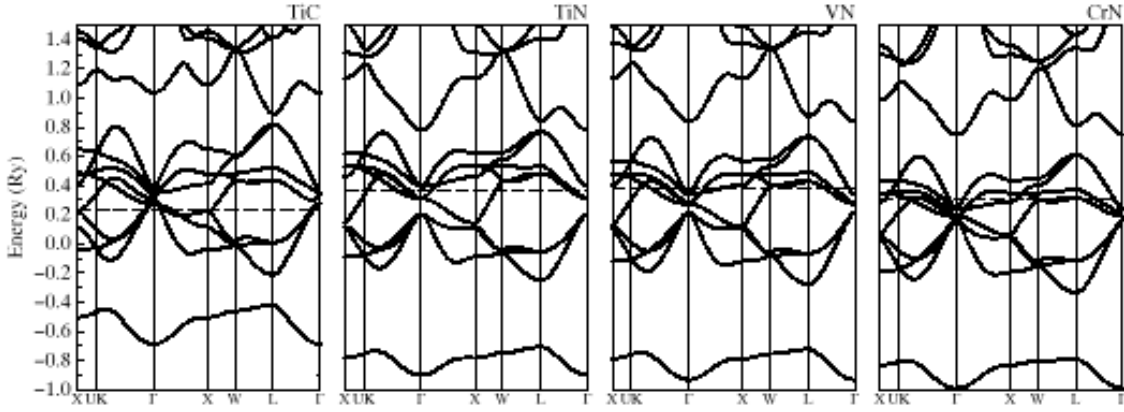


Fig. 1: Energy bands of TiC, TiN, VN and CrN calculated in the local density approximation using the FP-LMTO method.

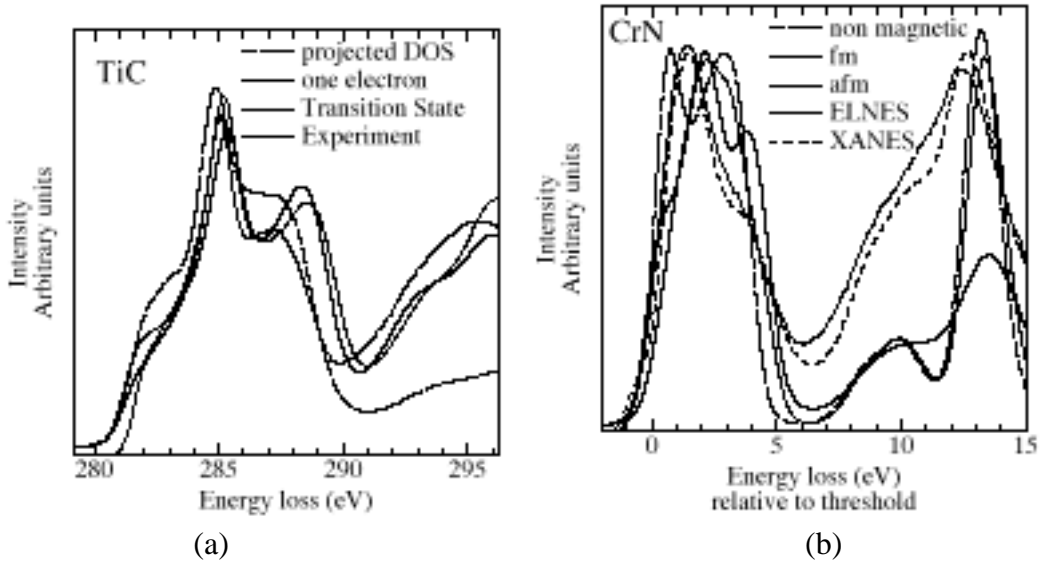


Fig. 2: (a) The experimental anion K-edge ELNES in TiC superimposed on three theoretical estimates of the spectra. (b) The experimental anion K-edge ELNES and XANES in CrN compared with the Mulliken projected N 2p densities of states in various magnetic configurations.

## **Mn doping in GaAs**

M. van Schilfgaarde

### **Motivation:**

Recently, it was shown that Mn doped GaAs ( $< 5\%$  Mn) undergoes a transition to a ferromagnetic state for  $T < 100\text{K}$ . Yet very little is understood about the material, the magnetic exchange interactions, or possible applications.

Accomplishments

### **Accomplishment:**

A theoretical study of the thermodynamics and the corresponding exchange interactions of Mn incorporation into III-V compounds is in progress. Several important pieces of information have emerged to date:

The exchange coupling is very strong for nearest neighbor interactions, but much weaker for more distant interactions. This leads us to predict that there is a strong tendency for the Mn to cluster into small nanoclusters of several (3 or 4) magnetic atoms. Thus the magnetic state, and the critical temperature do not correspond to the usual transition from a FM state to a paramagnetic state, but a rather a 'blocking' temperature in which the nanoclusters remain ferromagnetically aligned, but the nanoclusters themselves are paramagnetic (superatoms).

There is a strong non-Heisenberg component to the coupling, including three-body and higher order interactions. Particularly in the nitrides, the coupling consists largely of a Zener-like exchange derived from the higher lying  $t_{2g}$  levels in competition between the dominant (FM) Zener exchange and an antiferromagnetic Anderson superexchange derived from the lower  $e_g$  levels. The  $t_{2g}$  levels are slightly more than half filled.

The coupling is about twice larger in the nitrides than in the arsenides. Thus the nitride-based DMS are predicted to have much higher Curie temperatures.

### **Significance:**

The marrying recent developments in magnetism with semiconductor technology is emerging as one of the new frontiers in both subjects. Theoretical predictions such as those indicated above rapidly contribute to a much needed basic understanding of the key materials properties, and suggest new ways to achieve or enhance desired properties, such as a semiconductor based "spin filter."

### **Publications:**

A manuscript is in preparation for submission to Physical Review Letters.

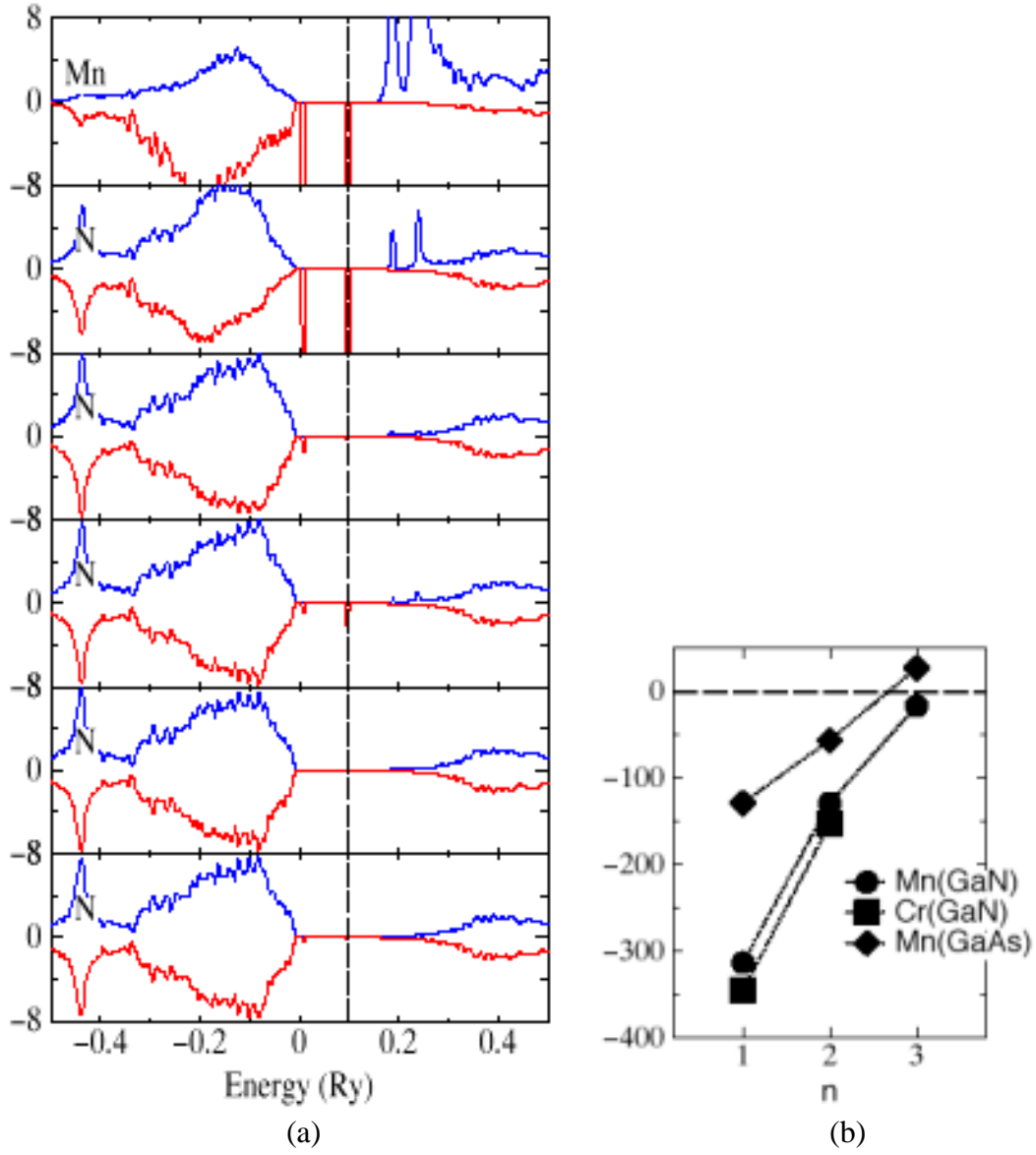


Fig. 1: (a) Density-of-states resolved into sites near a Mn impurity embedded in a GaN host. Red and blue lines are for majority and minority spins respectively. Majority spin defect levels can be seen in the gap. Successive panels show DOS at N sites successively farther from the impurity. (b) Heat of reaction for:  $\text{Mn}_n \text{Ga}_{108-n} \rightarrow (\text{Mn}_{n+1} \text{Ga}_{108-n-1} + \text{Mn}_{n-1} \text{Ga}_{108-n+1})/2$ . The minimum energy cluster size corresponds to where energy crosses zero ( $n=3$ ).

## Generalizations of Peierls-Nabarro Model

M. van Schilfgaarde

### Motivation:

Understanding the relation between lattice geometry, interatomic interactions and dislocation structure is one of the fundamental problems of dislocation theory. The Peierls-Nabarro (PN) model is a unique example of a highly tractable model that in principle provides a framework for establishing such a relation. The original PN model and methods of its solution, however, suffer several shortcomings: (i) it possesses an inconsistent ("continuum") representation of the misfit energy; (ii) the misfit energy is approximated in terms of the generalized stacking fault energy (GSF); and (iii) simple and tractable solutions are known only for a model restoring force law.

### Accomplishment:

We demonstrate that each these problems can be overcome to some degree without significant loss of tractability and physical transparency of the original PN model. Moreover, we present a rigorous and physically transparent analysis (within the PN model) of the relation between characteristics of the GSF geometry/energetics and two dislocation structure parameters: the partial width  $w$  and the partial separation  $d$ . Using trial functions<sup>1</sup> and a variational principle, consistency of the misfit energy representation is restored without loss of tractability. We propose a "modulated GSF" (MGSF) to describe more accurately misfit energy. To date we have applied the MGSF approach with a model interatomic potential, showing that it much better approximates the misfit energy than the traditional GSF. We apply these theoretical findings for fcc metals (Al, Ir, Au) and intermetallics (Ni<sub>3</sub>Al, Ni<sub>3</sub>Ge, NiAl, TiAl) and CuAu alloy with GSF and MGSF's calculated within the local-density approximation using the full-potential linear muffin-tin orbital method (FLMTO).

### Significance:

Understanding the core structure of dislocations, and their motion under stress is fundamental to a material's mechanical properties. The present approach much more closely approximates a rigorous quantum-mechanical description of the dislocation while retaining the physically intuitive and computationally tractable character of the PN model.

### Publications:

Talks will be presented at the spring MRS meeting and the dislocations-2000 workshop.

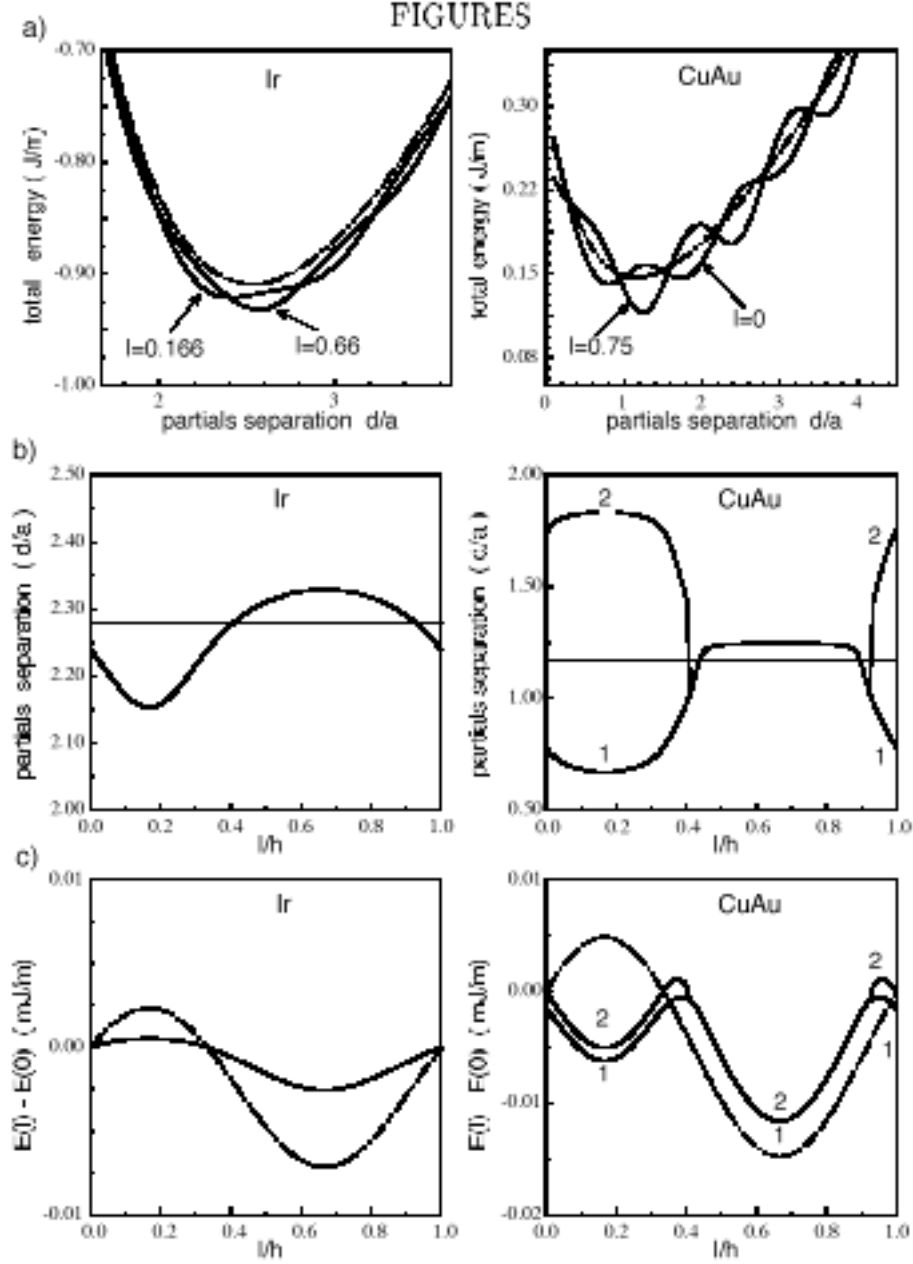


FIG. 1 Dislocation energy (in J/m) as a function (a) of the partials separation  $d$  and (b) a corresponding dependence of  $d$  on  $l$  (in case if more then one stable core configuration exist, solution which are close in energy and numbered as “1” and “2”) and (c) a corresponding dependence of the total energy on the position of the ordinary dislocation center give by  $l$  in interplanar distance  $h$  units. All these dependencies calculated for Ir (left panel) and CuAu (right panel), the ones determined within the “continuum” approximation used in the original PN model are presented by the dotted-dashed lines.

## Electronic Structure Methods Development

M. van Schilfgaarde

### **Motivation:**

Electronic and mechanical properties of materials ultimately depend on the electronic structure. Thus, the ability to calculate the electronic structure and derivative properties from first principles is of fundamental importance to a fundamental understanding of them and their control. The local-density approximation (LDA) has proved to be a powerful parameter-free, first-principles approach to the prediction of a wide range of materials properties, such as heats of formation optical excitation spectra, crystal structure and vibrational properties. Existing implementation of the LDA are (1) limited limited to relatively small scale by computational bottlenecks, and (2) inexact because of the local approximation.

### **Accomplishment:**

A new all-electron implementation of the LDA was recently completed. To scale to large systems, it is necessary to have short-ranged, real-space orbitals. The central challenge here is to retain LDA quality precision while reducing the basis set to a minimal size. A tight-binding version of this code is in progress that will enable one to significantly increase the scale of materials accessible to calculation. It uses wave functions that are by construction tailored to the crystal potential and are thus to the “best possible.”

We also develop a new self-consistent tight-binding model which contains contributions to non-spherical potentials. Parameters are taken from ab initio calculations, and this approach enables us to analyse and and compare against experimental phase stabilities in terms of ionic versus covalent effects, including polarisation of the anions. It promises to be useful for rapid simulation of more complex systems.

### **Publications:**

M. Methfessel, Mark van Schilfgaarde, and R. A. Casali, “A full-potential LMTO method based on smooth Hankel functions,” Proceedings of the Workshop on the Tight-Binding LMTO Method, to appear as Springer “Lecture Notes in Physics,” ed. H. Dreysse.

M. W. Finnis, A. T. Paxton, M. Methfessel, and M. van Schilfgaarde, “Crystal Structures of Zirconia from First Principles and Self-Consistent Tight Binding,” Phys. Rev. Lett. 81, 5149 (1998).

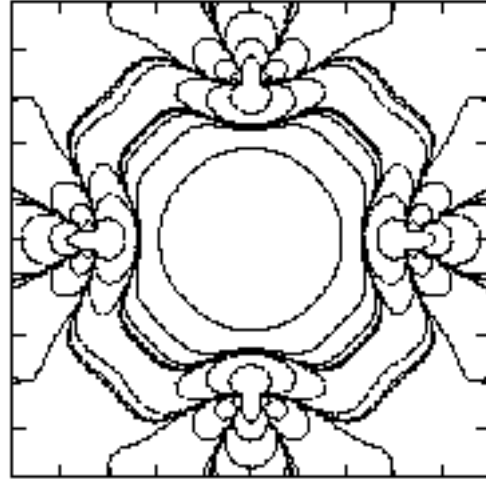
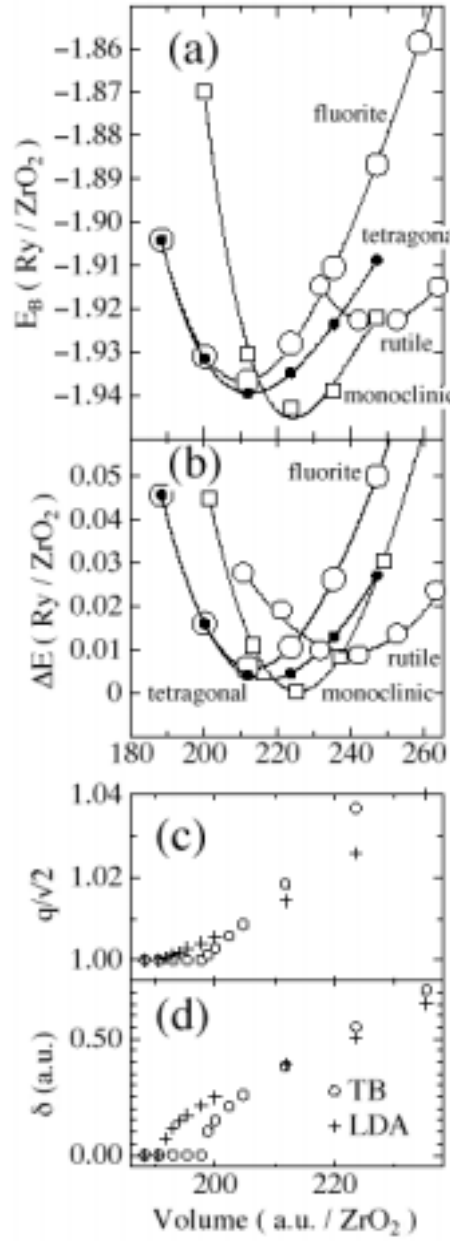


Fig. 1: Structural energy versus volume in four phases of ZrO<sub>2</sub>.  
 (a): ab initio (LDA) results  
 (b): empirical-tight binding with new nonspherical potentials.  
 (c) and (d): axial ratio and distortion parameter in the t modification ZrO<sub>2</sub> as a function of volume.

To Right: Illustration of a tight-binding orbital that is both short-range and accurate.

## Probing the mechanisms for self-assembly on metal surfaces: thermal fluctuations of the Au(111) herringbone reconstruction

O. Schaff, A.K. Schmid, J. de la Figuera, N.C. Bartelt, and R.Q. Hwang

### Motivation:

Dislocations on metal surfaces often self assemble to form complicated ordered networks with unit cell dimensions on the order of 10's of nanometers. Although many different types of dislocation networks have been observed and characterized, the energy balance that determines which network should form in any particular situation is still far from clear. Theoretical work at Sandia has shown that it is possible to *qualitatively* explain the internal structure of the dislocation networks with a simple two-dimensional Frenkel-Kontorova model, but whether or not this model is a *quantitatively* correct model for the energetics is not known. To check the accuracy of the Frenkel Kontorova model we have used variable temperature STM to measure directly the forces holding together the dislocation networks, and compared the result with the theoretical predictions.

### Accomplishment:

The prototypical example of a surface dislocation network is the Au(111) herringbone reconstruction. This network consists of lines of Shockley partial dislocations arranged in a herringbone pattern with an 8 x 30nm unit cell. Each herringbone unit cell contains two simple edge dislocations, one at each of the "elbows" of the herringbone pattern. An atomic resolution STM image of three such dislocations is shown in Figure 1.

At temperatures just above room temperature, Au atoms are randomly exchanged in and out of the dislocation cores. This is evident from the apparent "fuzziness" of the edge dislocation cores in the STM image taken at 80°C shown in Fig. 1. This random exchange results in random motion of the position of the cores. We can track this motion, atom by atom, as shown in Fig. 2. The motion of the dislocations is constrained by the repulsions between the cores. Figure 3 shows that the thermal distribution of distances between the cores is approximately Gaussian.

This Gaussian distribution suggests that the interaction between the cores is approximately harmonic, i.e., they can be quantified by a simple spring constant. From the width of the measured Gaussian we estimate that this spring constant is  $2.5 \pm 0.2 \text{ meV/\AA}^2$ . This is in almost perfect agreement with the value of  $3.0 \text{ meV/\AA}^2$  predicted by the theoretical Frenkel-Kontorova model that we have constructed to reproduce the observed structure of the herringbone reconstruction.

### Significance:

From a combination of theory and experiment, we have shown that the 2-D Frenkel-Kontorova model provides an accurate, quantitative description of the energetics of the Au(111) herringbone reconstruction. This is significant because such reconstructions are often proposed as templates for the growth of useful nanostructures.

### Publications:

*Measuring the interaction between edge dislocations in the Au(111) herringbone reconstruction* by O. Schaff, A.K. Schmid, J. de la Figuera, N.C. Bartelt, and R.Q. Hwang, presented at the AVS International Conference in Seattle, Oct. 1999, and to be published.

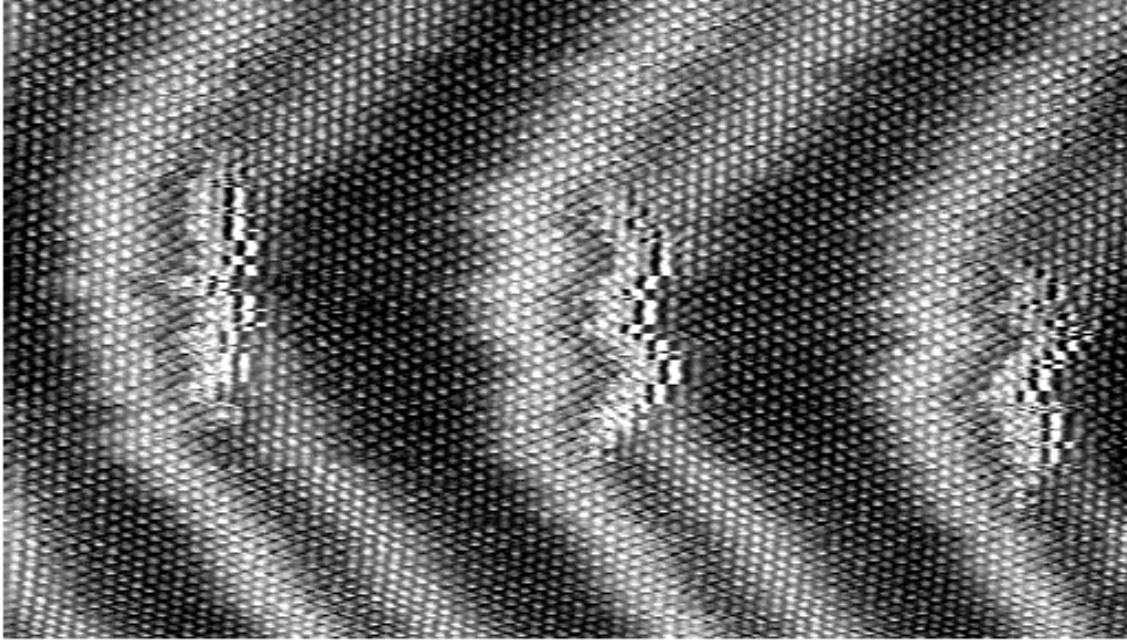


Figure 1: Atomic resolution STM image of fluctuating edge dislocations in the Au(111) herringbone reconstruction at 80°C.

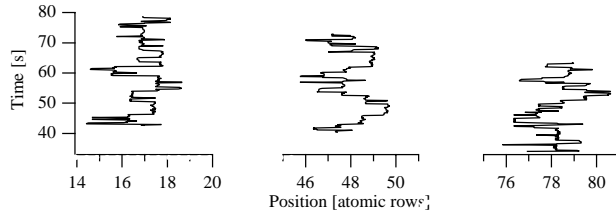


Figure 2: Atom-by-atom chart of the change in position of the dislocations shown in Figure 1.

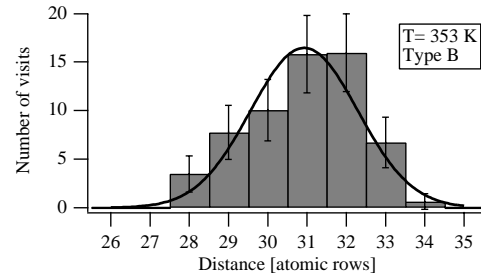


Figure 3. Histogram of distances between edge dislocations. The fit shows a Gaussian fit. The width of the Gaussian provides an estimate of the strength of the harmonic interactions between dislocation cores.

## Strain Effects on diffusion in FCC Metals

S. M. Foiles, Anton van der Ven, M. D. Asta

### Motivation:

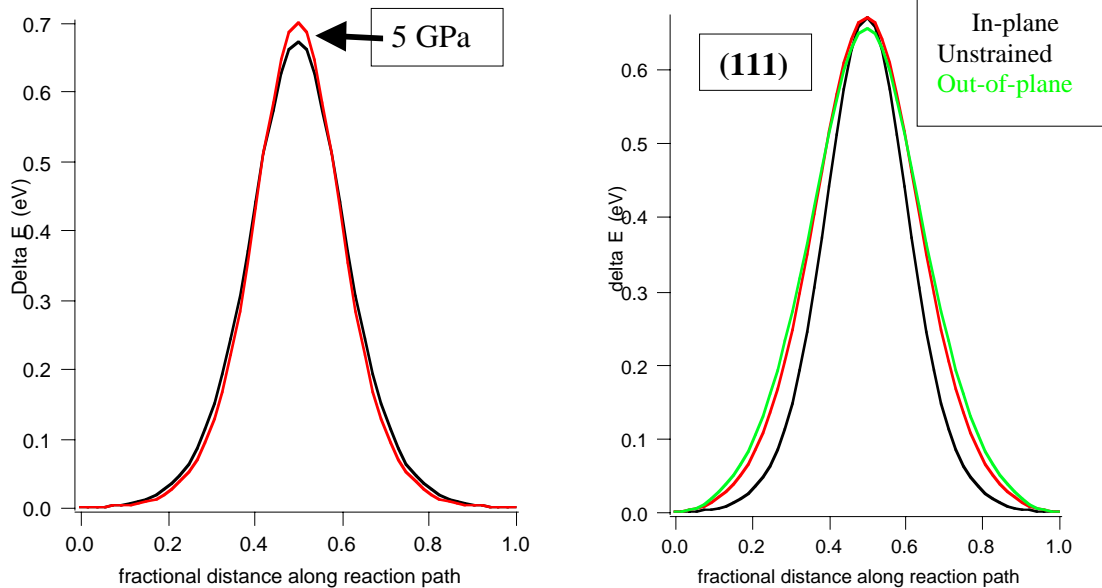
There is significant interest in the structure, stability and growth of thin film structures. It is known that these structures can have substantial stresses. The goal of this work is to determine whether these stresses can substantially modify diffusivities in these structures for a typical fcc metal, Cu. This work complements the active research on stress effects on diffusion in the semiconductor materials. The latter topic is of interest to the electronics industry where indications of such effects have been observed.

### Accomplishment:

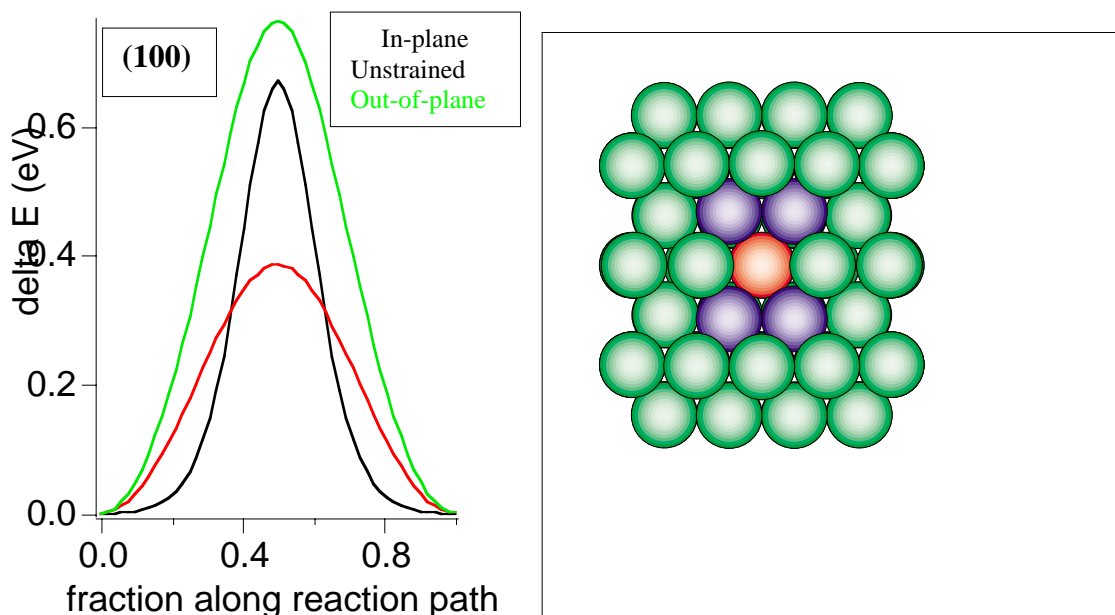
The energetics associated with vacancy diffusion in Cu have been computed as a function of the stress state. The majority of the calculations were performed using the embedded atom method (EAM) with selected results confirmed using *ab initio* electronic structure calculations based on density functional theory. The vacancy formation energies, vacancy migration energies and activation volumes determined from the *ab initio* calculations are all in good agreement with the known experimental values of these quantities. Calculations for uniform compression and dilation indicate that the activation energies for diffusion should be only weakly affected by hydrostatic pressure in agreement with experimental observations. Activation energies were then computed for various strained configurations. This allows for the determination of the elastic dipole tensor associated with the equilibrium and activated states. This provides the quantities needed to compute the change in activation energy for an arbitrary strain state as long as the system is in the elastic regime. While most strain states were found to have only mild effects on the vacancy migration energy, an interesting result was obtained for the case of plane strain in the (100) direction. It was found that for this case that substantial anisotropy in the diffusion behavior is obtained. For the case of 2 GPa compressive stress in the (100) plane at 500 K, the diffusivity within the (100) plane is 48 times larger than normal to the plane. These stress levels are not uncommon in thin film systems. This suggests that diffusion in such systems could be substantially anisotropic. The origin of this effect can be understood in terms of the geometry of the transition state combined with the expansion in the direction normal to the (100) plane due to the Poisson effect. As shown in the figure, the expansion along [001] relieves the geometric bottleneck for diffusion within the (001) plane but not for diffusion out of that plane.

### Significance:

There is a substantial literature on the effect of stress on diffusion in thin films. This work, though, focuses primarily on the effect of the stress on the driving forces for diffusion. It is generally assumed that the diffusivities are not changed by the presence of the stress fields. This assumption is justified by the small change in diffusivities caused by hydrostatic pressure. This work shows that the assumption of constant diffusivities in modeling of stress in thin films may be substantially incorrect for some systems. This point has been realized recently with regard to diffusion in semiconductor systems. The present work demonstrates that similar problems can arise in metallic systems.



The energy along the reaction pathway for vacancy diffusion. The left panel shows the small effect of a hydrostatic pressure of 5 GPa. The right panel shows the effect of a 3.5% in plane compression in the (111) plane.



The left panel shows the effect of 3.5% compression in the (001) plane on the activation energies for diffusion. Note that diffusion hops within the (001) plane are favored. The right panel shows the transition state geometry viewed along [110], the direction of motion of the atom. The red atom is the migrating atom and the blue atoms are the 4 atoms that form the bottleneck at the transition state. Note that the expansion of the system in the vertical, [001], direction that results from the in-plane compression eases the bottleneck.

## Predicting strength from microstructure

<sup>1</sup>D.A. Hughes and N. Hansen<sup>2</sup>

<sup>1</sup>SNL/CA, <sup>2</sup>Risø National Laboratory, Denmark

### Motivation:

New tools for characterizing and analyzing microstructures have been developed in the last five years which create a firmer basis to explore the relationship between microstructure and flow stress. A central question regards the identification of the different microstructural elements, their relative strength contributions and persistence from small to large strain deformation.

### Accomplishment:

A quantitative microstructural analysis was performed on pure polycrystalline nickel (99.99%) cold rolled to reductions including 10, 20, 70, 90 and 98% ( $\epsilon_{vM}$  0.1 to 4.5). Applying transmission electron microscopy (TEM) techniques key structural parameters, such as spacing between dislocation boundaries and high angle boundaries, as well as the misorientations across their boundaries, have been measured and analyzed. Application of scaling and similitude hypotheses to these microstructural parameters and their distributions revealed that the structures are homologous with increasing strain. This similar behavior indicates that the measured parameters capture the important features of the structure. The following conclusions are reached. The key structural element is a cell block, composed of cell block boundaries (GNBs) and cell boundaries (IDBs) (Figure 1). For both types of boundaries, boundary spacing and width decreases and the misorientation angle increases with increasing strain. Saturation of these parameters was not observed. Taking all the measurable structural parameters: spacing, misorientation angle, and dislocation density, and assuming additive strength contributions, we derive from Hall-Petch and dislocation strengthening flow stress predictions which are in good agreement with the stress values and hardening rates observed experimentally (Figure 2). No saturation of the calculated or experimental flow stress was observed.

### Significance:

Scaling and similitude provide governing principles for structure formation. Based on this structural information and a detailed description of the morphology, structural parameters are identified, strength determining parameters chosen, and strength-structural relationships obtained. The suggestion is then made that two strengthening contributions should be considered: (i) dislocation strengthening due to the presence of low angle boundaries and (ii) grain boundary strengthening due to medium to high angle boundaries. The calculated individual strength contributions evolve differently with the strain and their addition leads to flow stress values and hardening rates in good agreement with those observed experimentally.

### Publications:

N. Hansen and D. Hughes, "Microstructural Evolution and Hardening Parameters," in press *Mater. Sci. and Eng.*, (March 1999).

D. A. Hughes and N. Hansen, "Microstructure and Strength of Nickel at Large Strains," submitted to *Acta Mater.*, November 1999.

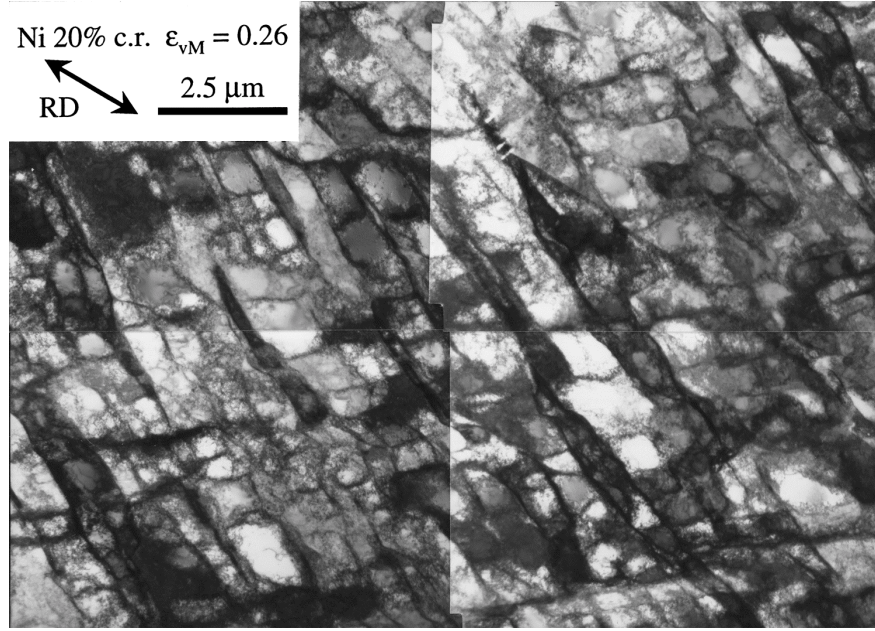


Figure 1: TEM micrograph of cold rolled pure nickel illustrating nearly planar extended GNBs surrounding more equiaxed cells to form cell blocks.

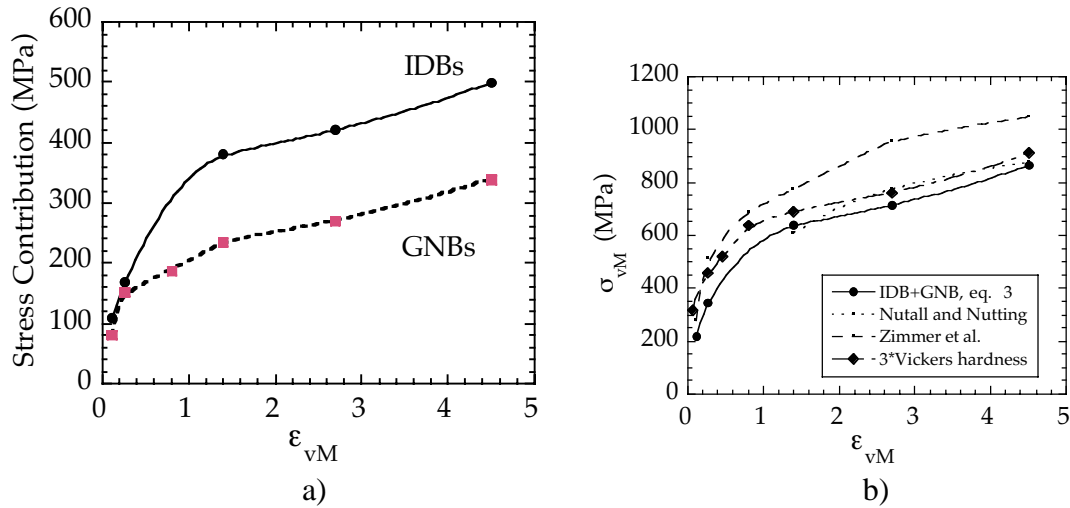


Figure 2: a) The strength contribution of IDBs is based on dislocation strengthening, while that of the GNBs is based on Hall-Petch strengthening. Both types of boundaries contribute to linear hardening at large strains above 1.5. b) Stress predictions based on the combined microstructure match the level of hardness measurements on the same samples and stress strain data from the literature. Note in particular the agreement in the strain hardening that changes from parabolic at small strain to linear at large strain.

## **Stacking Fault Energy and Microstructure Effects on Torsion Texture Evolution**

Darcy A. Hughes<sup>1</sup>, Ricardo Lebensohn<sup>2</sup>, H. R. Wenk<sup>3</sup>, and Ashish Kumar<sup>4</sup>

<sup>1</sup>SNL/CA, <sup>2</sup>Univ. of Rosario, Argentina, <sup>3</sup>Univ. of California, Berkeley, <sup>4</sup>Brown Univ.

### **Motivation:**

The formation of a preferred crystallographic texture during deformation of metals causes mechanical and magnetic property anisotropy. This formation is further modified by the concurrent microstructure evolution. Understanding the roles of dislocation slip versus deformation twinning in the formation of texture and microstructure are pertinent for the prediction and control of material anisotropy in metal industries from cars to magnets.

### **Accomplishments:**

A series of experiments and simulations that vary the crystallographic texture and microstructure simultaneously were performed to establish the role of the microstructure in texture formation in fcc metals. The stacking fault energy of the metal (SFE) which is known to have a strong impact on texture and microstructure is the vital parameter used to make these variations. Torsion deformation was chosen to isolate the role of slip. It was determined that the wide variety of textures and microstructures observed as a function of SFE and temperature were developed by slip processes alone; twinning was not necessary, as previously thought (Figure 1). The different textures are caused by: i) variations in local slip patterns within a single grain as revealed by grain subdivision into differently deforming cell blocks and ii) more subtly by the cell block shape. The local selection of slip systems creating the lattice rotations within a cell block is altered by the planarity of slip. Slip planarity is controlled by the SFE and temperature. It is hypothesized that the newly observed texture components, that are distinct from the generally accepted ideal components, are created by the different slip processes occurring as a result of low SFE and low temperature. A more subtle effect of grain subdivision is related to the cell block shapes that develop as a function of SFE and temperature and correspond to the different textures observed. The shape of the cell block is related to the level of constraint required by the deformation. The slip pattern changes and cell block shapes correlate with the presence or absence of certain ideal texture components whose evolution is not simulated. Materials and conditions with similar deformation microstructures developed similar textures in the experiments.

### **Significance:**

The different slip patterns formed within a single grain are at odds with the central Taylor assumption. How well the Taylor assumption is fulfilled on average depends on the SFE and deformation temperature as clearly shown by the development of new texture components. Future refinements of polycrystal plasticity simulations will need to include the characteristics of the microstructure. Clearly a grain cannot be considered as a homogeneous unit in realistic models of the deformation process.

### **Publications:**

D. A. Hughes, R. Lebensohn, H. R. Wenk, and A. Kumar, "Stacking Fault Energy and Microstructure Effects on Torsion Texture Evolution," *Proc. Roy. Soc. London*, in press, (1999).

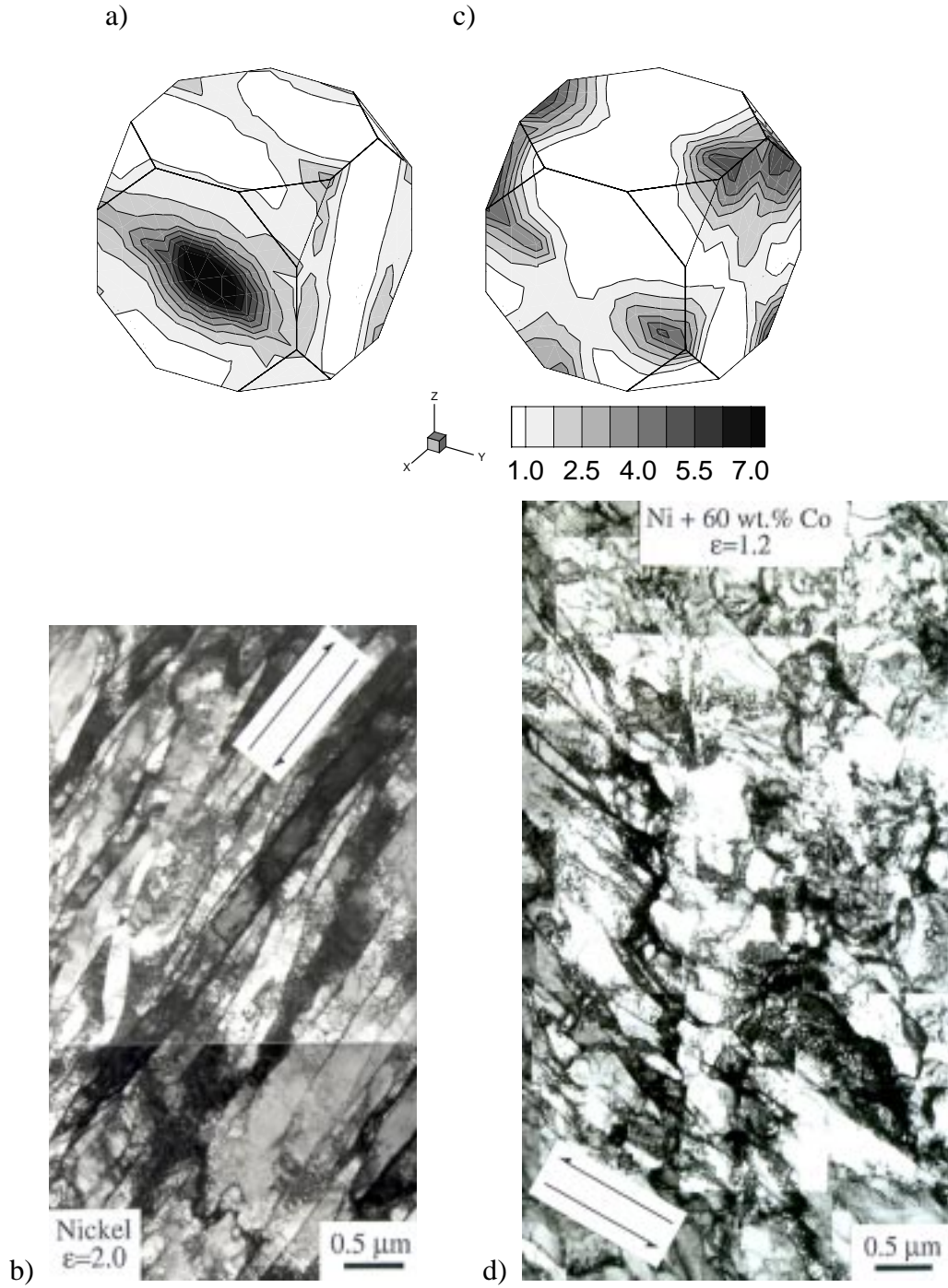


Figure 1. a) Crystal orientation distribution function (CODF) plotted in the fundamental zone of Rodrigues space (Frank, 1988) showing a  $\{100\}\langle 1\bar{1}0\rangle$  preferred orientation (darkest shading) and b) a transmission electron micrograph of long cell blocks for nickel following torsion deformation to a von Mises effective strain  $\epsilon=2$ . c) CODF showing a  $\{\bar{5}42\}\langle 652\rangle$  preferred orientation (darkest shading) and d) TEM micrograph of the more complex dislocation structure (few twins) for Ni+60 wt.% Co following torsion deformation to  $\epsilon=1.2$ .

## Short-range Order in Dislocation Boundary Structures

M.C. Bartelt and D.A. Hughes

### Motivation:

Extended dislocation boundaries induced by deformation present obstacles to subsequent plastic flow. Thus it is only natural that their characteristic spacing be viewed as an intrinsic measure of the mechanical strength of strain-hardened materials. This parameter is also useful to discriminate between models of flow stress, some of which postulate, instead, the existence of a continuous range of relevant length scales. However, information on the characteristic boundary spacing alone is insufficient to predict subsequent material flow and shape changes, which are strongly affected by anisotropies introduced by the deformation process. A more detailed characterization of dislocation boundary structures is achieved by analyses of the full distribution of boundary spacings (done in Ref.1), and of spatial correlations in the positions of the boundaries.

### Accomplishments:

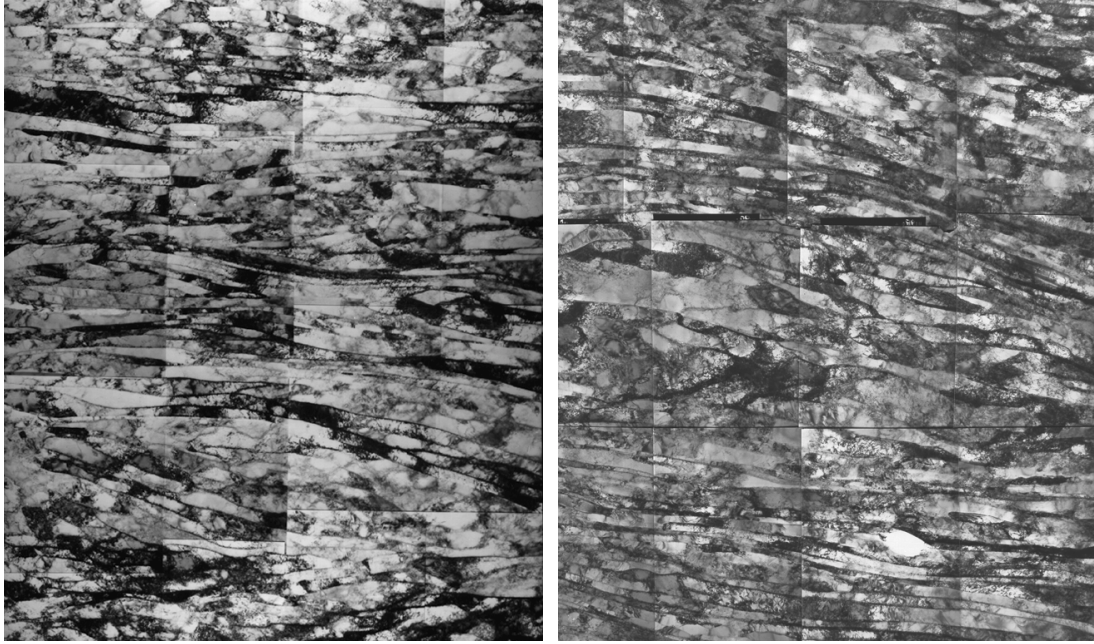
The pair correlations are the most basic of the correlation functions, and can be obtained directly from traces of the individual extended dislocation boundaries (or GNBs) found in the TEM images; see Fig.1. The pair correlation function is generally defined as the probability that two sites on this trace, at a given distance, have the same pixel color (e.g. black for dislocation-rich and white for dislocation-poor). To expose possible non-random features, this probability is typically normalized by its value at large separations (where the colors of the two sites are uncorrelated). So the pair correlation function vanishes at large separations. The basic form of the pair correlations obtained for cold-rolled nickel is shown in Figs.1(e)-(f). For pairs of sites selected in the direction perpendicular to the boundaries, our analysis reveals a depletion zone near the boundaries, where the probability to find another boundary is lower than it would be if the boundaries were randomly spaced; see Fig.1(f). The width of this zone scales like the characteristic boundary separation,  $D$ . For separations near  $D$ , for which one of the sites is likely to fall in the gap between two boundaries, the pair-correlation function goes through a negative minimum; see Fig.1(f). It is this deviation from zero that characterizes the degree of short-range order in the spatial arrangement of the dislocation boundaries. In contrast, there is no obvious ordering in the direction parallel to the boundaries, the direction of easier material flow; see Fig.1(e).

### Significance:

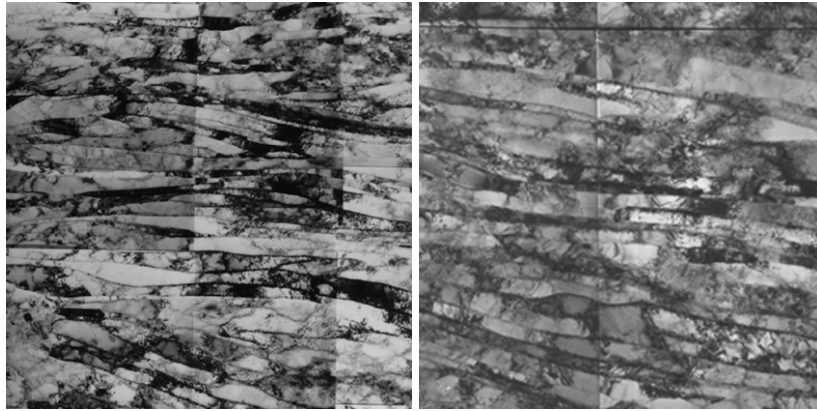
The full distribution of GNB spacings (Ref.1) has shown that these can deviate from the average spacing,  $D$ , by as much as a factor of 5, but says nothing about how small and large boundary spacings mix. For this information, one must consider pair (and other many-point) spatial correlations. Our pair-correlation analysis confirms, unambiguously, the existence of a characteristic scale proportional to  $D$ . But it also reveals short-range order in the arrangement of the boundaries, as if they effectively “repelled” each other at short separations. These results are most useful to model nucleation of new boundaries between other boundaries, and coalescence of nearby pairs of boundaries, during deformation.

### Publications:

1. Scaling of the spacing of deformation-induced dislocation boundaries, A. Godfrey and D.A. Hughes, *Acta Materialia*, in press.
2. Anisotropy and short-range order in dislocation boundary structures, M.C. Bartelt and D.A. Hughes, in preparation.



(a)  $6.5 \times 8 \mu\text{m}^2$ : 90% cr,  $e_{vM}=2.7$ ,  $D=0.21 \mu\text{m}$  (b)  $6.5 \times 8 \mu\text{m}^2$ : 98% cr,  $e_{vM}=4.5$ ,  $D=0.13 \mu\text{m}$



(c) (20Dx20D): 90% cr

(d) (20Dx20D): 98% cr

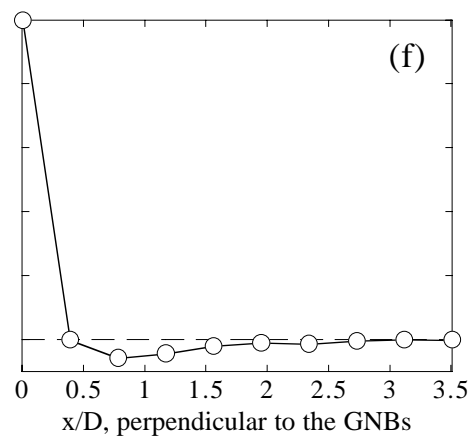
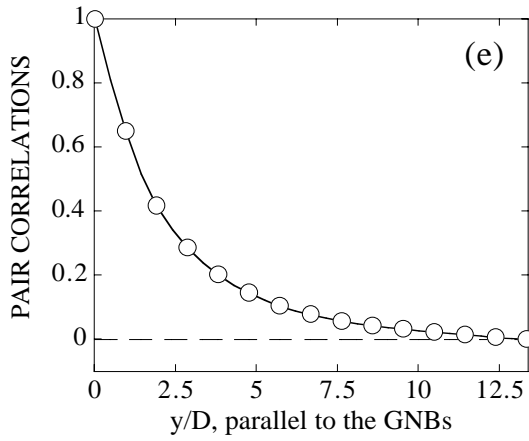


**Fig. 1** - TEM images of a high-purity (99.99%) nickel polycrystal (grain size: 80-100 $\mu\text{m}$ ) deformed by cold-rolling to (a),(c) 90% and (b),(d) 98% reduction. (c),(d) On a scale set by D, the two systems are statistically indistinguishable. (e),(f) Pair correlation functions.

## Factorization of Correlations in Dislocation Structures

M.C. Bartelt and D.A. Hughes

### Motivation:

At sufficiently high strains, extended dislocation boundaries formed during deformation organize into fine lamellar-like structures; see Figs.1(a)-(b). The minimum set of dynamical rules that support such order has not been identified, nor have conventional models of (many-) dislocation interactions been able to reproduce it. A different way to approach these issues is to develop master equations for the evolution of the distribution of linear spacings (or “gaps”) between the extended dislocation boundaries, accounting for such processes as nucleation of new boundaries, coalescence of nearby pairs of adjacent boundaries, or removal of boundaries due to crystal rotations into coincidence, as suggested by experiment. Difficulties arise because these equations couple to a full hierarchy of spatial correlations. For instance, the rate of coalescence of pairs of adjacent boundaries, which affects the probability of finding a pair of boundaries at a certain distance (or a gap of a certain size), depends on the probability of finding triplets of adjacent boundaries (or pairs of gaps). Consequently, the ease with which these evolution equations can be solved relies on some knowledge of the form of these higher-order correlations, and then on the ability to truncate that hierarchy at some level, using factorization of the joint probabilities. It is thus important and useful to verify to what extent such property holds for experimental distributions of dislocation boundaries.

### Accomplishments:

In Fig.1(c), we show data for the joint probability (averaged over many adjacent pairs of boundaries),  $P(d_1, d_2) = P(d_2, d_1)$ , of finding two adjacent gaps (or spacings) of linear size  $d_1$  and  $d_2$ , measured perpendicular to the extended boundaries in Fig.1(b). Clearly, one is unlikely to find gaps between boundaries much larger than the average spacing,  $D$ , consistent with the expectation that new boundaries are likely to form in those (plastically soft) regions during deformation. Consequently, there are also very few pairs of large adjacent gaps between boundaries. Detailed inspection of cross-sections of the data for the joint probability  $P(d_1, d_2)$  versus  $d_2$ , for selected  $d_1$  values, reveal sub-distributions that look very much like the single-gap function  $P(d_2)$ . This result suggests that, to good approximation, the relation  $P(d_1, d_2) \approx P(d_1)P(d_2)$  is satisfied in experiment, i.e., on average the sizes of two adjacent gaps between boundaries do not depend strongly on each other; see also Ref.1 for misorientation-spacing correlations. That result holds in particular when one of the gaps is small (compared to  $D$ ), as is relevant for boundary coalescence; Fig.1(d).

### Significance:

This is a powerful result: the higher-order spatial correlations are approximately determined given the form of the single-gap function,  $P(d)$ . We are currently further testing this feature in simulations of the dislocation boundary formation process. Here we can directly compare full separation distributions of dislocation boundaries generated using the joint probabilities,  $P(d_1, d_2)$ , with those generated using the factorized probabilities,  $P(d_1)P(d_2)$ .

### Publications:

1. Distributions of Low and High Angle Boundaries in Deformed Metals, D.A. Hughes, in Recrystallization '99, Proceedings of The 4th International Conference on Recrystallization and Related Phenomena, ed. T. Sakai and H.G. Suzuki (Sendai, Japan: JIMIS, 1999) p.111-118.
2. Markov-chain models for dislocation boundary structures, M.C. Bartelt and D.A. Hughes, in preparation.

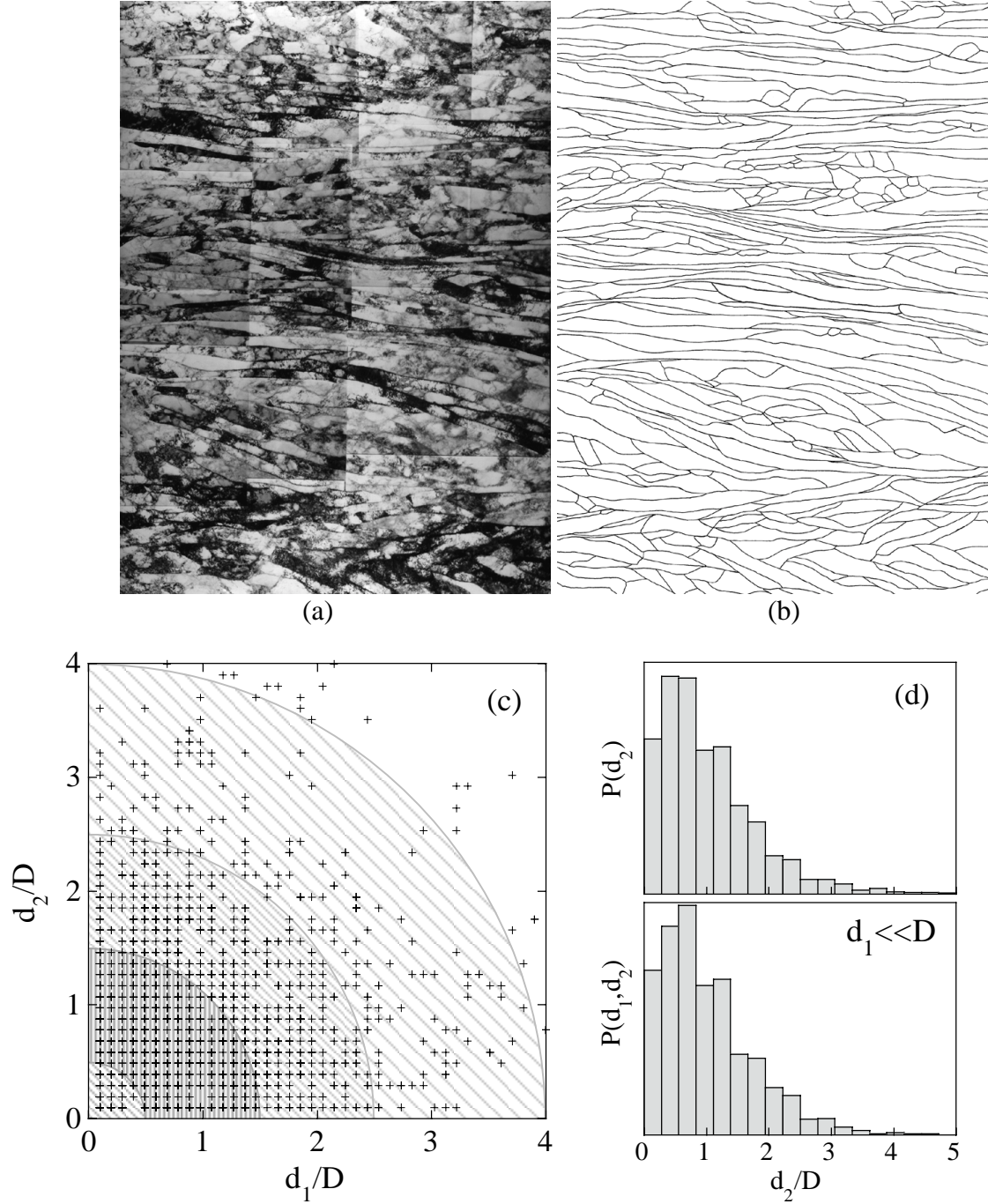


**Fig.1** - TEM image ( $6.5 \times 9 \mu\text{m}^2$ ) of a high-purity (99.99%) nickel polycrystal (initial grain size  $\sim 100 \mu\text{m}$ ) deformed by cold-rolling to 90% reduction ( $\epsilon_{\text{VM}} \approx 2.7$ ). The image shows contrast from a configuration of extended boundaries nearly parallel to the rolling direction ( $11^\circ$  off the horizontal), as is typical at this strain. They are on average  $D \approx 0.2 \mu\text{m}$  apart, and each accommodates an average crystal misorientation of  $15^\circ$ . They enclose blocks of cells of lower dislocation density and different characteristic scale. In (b), we traced only the extended boundaries. (c) The symbols are observed pairs of adjacent gaps between boundaries, and the shaded regions give a coarse-grained projected view of the value of the average joint probability,  $P(d_1/D, d_2/D)$ , for adjacent gaps (darker shade has higher value). (d)  $P(d_1 < D, d_2) \approx P(d_2)$ , which is relevant to describe coalescence of nearby boundaries.

# Dislocation-Based Model for the FCC to 9R Reconstruction at a $90^\circ\{111\}/\{211\}$ Boundary in Gold

D.L. Medlin and D. Cohen

## Motivation:

It has been known for over a decade that interfaces in low stacking fault energy (SFE) metals such as gold and copper can dissociate into complex, three-dimensional structures composed of arrays of stacking faults. Nevertheless, the factors controlling the geometry and distribution of faults, particularly in relation to the bounding crystal orientation, are still unclear. In recent work we have employed a partial dislocation based model to successfully describe and predict the specific stacking configuration at boundaries near the crystallographically simple  $\Sigma=3$  orientation [D.L. Medlin *et al.*, Acta Mater. 46(14) (1998) 5135; Materials Sci. Forum 294-296 (1999) 35]. This motivates us to test whether such a model can be extended to boundaries of more complex geometry.

## Accomplishment:

Figure 1 shows a lattice resolution TEM image of an interface in gold. The two grains are oriented relative to each other by a  $90^\circ$  rotation about their common  $\langle 110 \rangle$  axis, with the interface lying parallel to the vertical  $\{111\}$  planes in the left crystal. In the right crystal, the  $\{111\}$  planes run horizontally except in the vicinity of the interface where they bend slightly downwards. Careful examination of the planar stacking in this narrow region shows the presence of a stacking fault at every third plane. Such a fault distribution is equivalent to the so-called 9R phase, and in this regards the boundary dissociation is similar to the 9R reconstruction that has been observed previously in low SFE  $\Sigma=3$   $\{211\}/\{211\}$  boundaries. In the  $\Sigma=3$  case, we have shown that the grain orientation and boundary structure are well represented by an array of negative  $90^\circ$  (**A** $\delta$ ) and positive  $30^\circ$  (**B** $\delta$  and **C** $\delta$ ) Shockley partial dislocations distributed on adjacent  $\{111\}$  planes in a ratio of  $n_{90}:n_{30}=1:2$  (specifically, a repeating sequence: ...**A** $\delta$  **B** $\delta$  **C** $\delta$ ...); the 9R stacking results when the oppositely signed dislocations separate. In contrast, the grain orientation of the present  $\{111\}/\{211\}$  interface (which is approximately a  $\Sigma=99$  orientation), is produced by Shockley partial dislocations distributed in a ratio  $n_{90}:n_{30}=2:1$  (specifically ...**A** $\delta$  **A** $\delta$  **B** $\delta$  **A** $\delta$  **A** $\delta$  **C** $\delta$ ...). As shown in Figure 2, separation of the positive  $30^\circ$  dislocations (**B** $\delta$  and **C** $\delta$ ) from the negative  $90^\circ$  dislocations (**A** $\delta$ ) transforms the right FCC crystal to the 9R stacking (*i.e.* ...abc/bca/cab...). Furthermore, the wall of  $30^\circ$  dislocations, acting as a low angle tilt boundary, would be expected to bend the planes in the dissociated region through an angle of  $6.7^\circ$ , which is consistent with the experimental observations.

## Significance:

In developing a thorough understanding of interfaces, we would like to know what the basic functional units of a boundary are and how these relate to interfacial behavior. By successfully describing the decomposition mode and geometrical features of the  $\{111\}/\{211\}$  interface, our work points to the importance of Shockley partial dislocations as elements of interfacial structure and provides a key step in testing whether general high angle grain boundaries can be understood in terms of arrays of such defects.

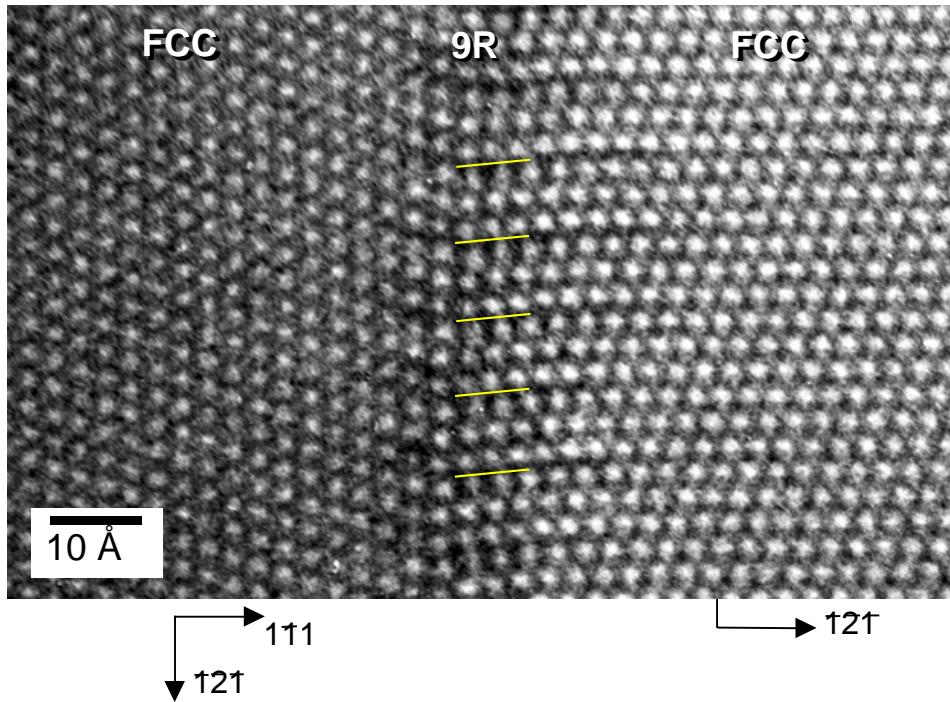


**Figure 1.** HRTEM image of  $\{111\}/\{112\}$  boundary in gold that has dissociated to form a narrow layer of material in the 9R stacking arrangement. The lines at the boundary, which are inclined at  $6.7^\circ$ , denote the positions of the stacking faults in the dissociated layer.

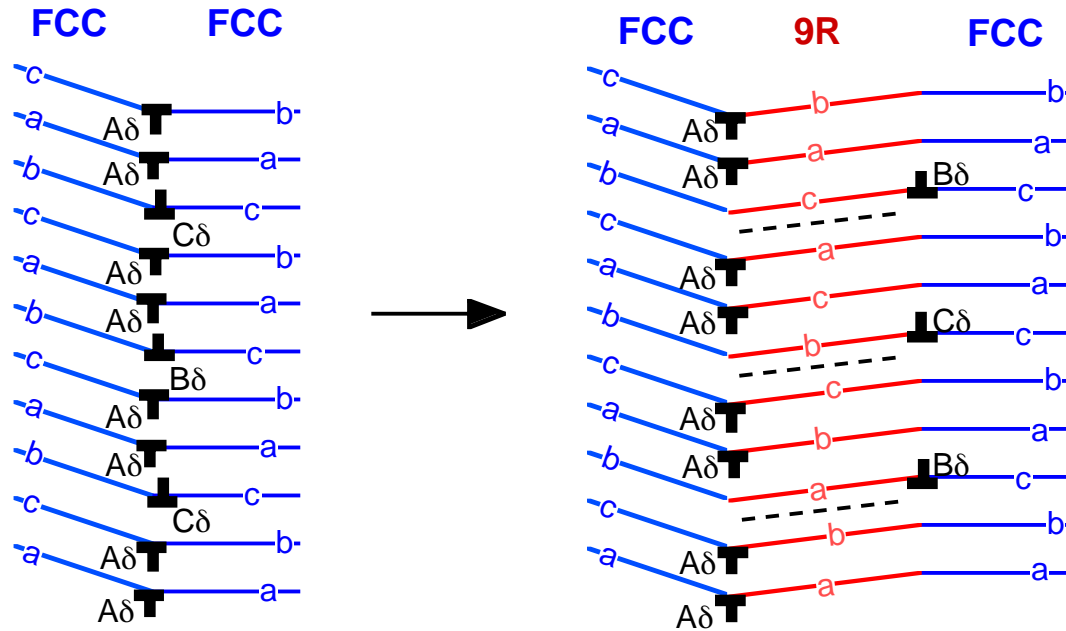


**Figure 2.** Model for formation of 9R phase through separation of the Shockley partial dislocations that comprise the interface. The model correctly describes the orientation relationship between the two FCC crystals and predicts a  $6.7^\circ$  inclination of the close-packed planes in the 9R layer, consistent with experimental observations.

## Determination of the Surface Structure of $\alpha$ - $\text{Al}_2\text{O}_3$ (0001)

C. F. Walters,<sup>1</sup> K. F. McCarty,<sup>1</sup> E. A. Soares,<sup>2</sup> and M. A. Van Hove<sup>2</sup>

<sup>1</sup>Sandia National Laboratories, Livermore, CA 94551

<sup>2</sup>Lawrence Berkeley National Laboratory, Berkeley, CA 94720

### Motivation:

Being the simplest and the only thermodynamically stable aluminum oxide,  $\alpha$ - $\text{Al}_2\text{O}_3$  is a prototype for understanding metal oxides. Because of this importance, sapphire surfaces have been extensively studied by experiment and theory. Nonetheless, a most basic property of its simplest clean surface, namely the structure of  $\alpha$ - $\text{Al}_2\text{O}_3$  (0001), remains controversial.

Determining the surface structure of a compound such as alumina is much more complicated than for a mono-atomic material. First, the (0001) surface can terminate in either a single Al layer, an oxygen layer, or a double Al layer (Fig. 1). In addition, the stacking periodicity at the surface may differ from that of the bulk. Finally, compound surfaces can potentially be phase-separated, i.e., consist of coexisting terraces having different stoichiometry or structure. The existence of a phase-separated surface may depend sensitively on processing conditions. Therefore, we have studied the  $\alpha$ - $\text{Al}_2\text{O}_3$  (0001) surface with particular emphasis on two issues – sensitivity to sample preparation and completeness of analysis.

### Accomplishment:

Using dynamical low-energy electron diffraction, we have determined the structure of the  $\alpha$ - $\text{Al}_2\text{O}_3$  (0001) surface. The diffraction results for 3 different preparations were analyzed using an exhaustive search of possible models, which included different terminations, mixtures of terminations, and stacking faults.

We conclude that the surface termination of  $\alpha$ - $\text{Al}_2\text{O}_3$  (0001) is a single Al layer, that the first interlayer spacing is significantly contracted with respect to the bulk spacing, and that the surface structure is insensitive to our different processing methods (Fig. 2). In addition, we have determined that the topmost Al atoms have unusually large vibrational amplitudes at room temperature.

### Significance:

We have resolved the contradictory experimental results regarding the termination of  $\alpha$ - $\text{Al}_2\text{O}_3$  (0001). More importantly, we provide the first experimental evidence for enhanced vibrations at an oxide surface. Such vibrations account for the substantial difference between the interlayer contractions determined by zero-temperature calculations and finite-temperature experiments. These large vibrations will have important implications for both the structural and chemical properties of alumina and other oxides and highlight the limitations of even state-of-the-art computations.

### Reference:

C. F. Walters, K. F. McCarty, E. A. Soares, and M. A. Van Hove, “The Surface Structure of  $\alpha$ - $\text{Al}_2\text{O}_3$  (0001) Determined by Low-Energy Electron Diffraction: Al Termination and Evidence for Anomolously Large Thermal Vibrations,” submitted to Phys. Rev. Lett. (2000).

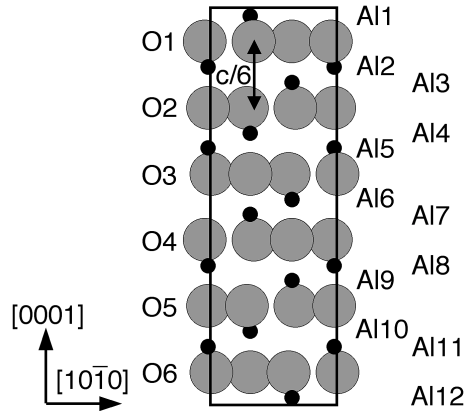


Fig. 1. Illustration of the 12 Al layers and 6 O layers, parallel to the (0001) surface, of the sapphire unit cell. The surface can be terminated by a single Al layer (i.e., Al1), an oxygen layer (O1), or a double Al layer (Al2+Al3).

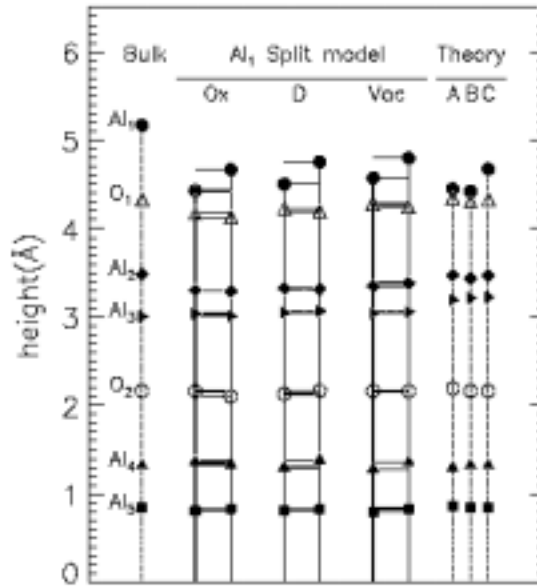


Fig. 2. Graphical representation of the atomic positions perpendicular to the  $\alpha$ - $\text{Al}_2\text{O}_3$  (0001) surface, for 3 different sample preparations, compared to bulk and theory. Because of the large vibrational amplitude of the topmost Al atoms, the surface must be modeled using the “split-atom” method. Physically, however, the Al atoms are at the average position. State-of-the art theory only models the system at zero temperature. Because of the anharmonic surface vibrations, significant expansion occurs at room temperature. Thus the theory overestimates the contraction of the outermost layer.

## Alloy Theory: Non-Configurational Entropies in Metallic Alloys

V. Ozolins, M. Asta

### Motivation:

Heat-treatment techniques and operating conditions of modern commercial alloys often involve high temperatures, where various contributions to the entropy strongly affect the thermodynamic stability of competing alloy phases. Traditionally, it has been assumed that the *configurational* entropy plays a dominant role in these phenomena. However, *non-configurational* entropy (e.g., magnetic, vibrational) can contribute significantly to the thermodynamic properties of alloy phases. We consider two technologically important systems where we find that the vibrational entropy effects exceed those of the configurational entropy.

### Accomplishment:

**Al-Cu:** This is a prototypical alloy system where precipitation hardening was first discovered. Al-Cu exhibits the following precipitation sequence: Solid solution  $\rightarrow$  GP1  $\rightarrow$  GP2  $\rightarrow$   $\theta'$   $\rightarrow$   $\theta$ . The  $\theta' \rightarrow \theta$  transformation is particularly important since it leads to a precipitous drop in alloy hardness.  $\theta'$  is a semicoherent, tetragonally distorted fluorite (prototype  $\text{CaF}_2$ ) structure, whereas  $\theta$  is a tetragonal *C16* ( $\text{Al}_2\text{Cu}$ ) structure. Since there is not much decrease in mechanical properties with the GP2  $\rightarrow$   $\theta'$  transformation, many industrial alloys are aged to produce  $\theta'$  precipitates. First-principles calculations done by C. Wolverton (Ford Motor Labs) show that the energy of the  $\theta'$  fluorite structure is lower than the energy of *C16*, in apparent disagreement with the observed precipitation sequence and the generally accepted view that *C16* is the ground state of  $\text{Al}_2\text{Cu}$ .

In collaboration with C. Wolverton, we have resolved this paradox by showing that the harmonic vibrational entropy of *C16* ( $\text{Al}_2\text{Cu}$ ) is considerably higher than the entropy of the  $\text{CaF}_2$ -type ( $\theta'$ ) phase of  $\text{CuAl}_2$  [ $S(\theta) - S(\theta') = +0.35k_B/\text{atom}$ ]. This vibrational entropy difference stabilizes *C16* ( $\text{Al}_2\text{Cu}$ ) above  $T \sim 500$  K, explaining the observed  $\theta' \rightarrow \theta$  precipitation sequence at typical aging temperatures. Currently, we are investigating the importance of the vibrational entropy for the stability of similar phases in other alloy systems.

**Al-Sc:** Scandium, when added to aluminum, is a powerful dispersion strengthener and grain refiner. For Al-rich compositions the solid-state portion of the Al-Sc phase diagram features two FCC-based phases with extremely narrow phase fields (see Fig. 2). The FCC-based Al solid-solution phase extends to roughly 0.2 at. % Sc at the eutectic temperature of 933 K. For more concentrated compositions a large two-phase field exists between the Al solid-solution phase and the ordered  $\text{Al}_3\text{Sc}$  compound possessing a cubic

FCC-based  $L1_2$  ( $\text{Cu}_3\text{Au}$ -prototype) crystal structure. Coherent precipitates of the latter phase are responsible for the excellent strengthening properties of Sc additions to Al.

### Significance:

In a previous first-principles study based upon the cluster-expansion method, M. Asta, S. M. Foiles, and A. Quong found that the measured solubility limits for Sc in FCC Al are significantly underestimated, as shown in Fig. 2. In particular, at the eutectic temperature of 933 K, measured and calculated solubility limits were found to differ by roughly a factor of thirty. It was hypothesized, based upon an analysis of the temperature dependence of the measured solubility limits, that this discrepancy could be attributed to the neglect of non-configurational entropy contributions to the Gibbs free energies of  $L1_2$  ( $\text{Al}_3\text{Sc}$ ) and of dilute Sc impurities in Al matrix.

Since then, we have incorporated vibrational contributions to the Gibbs free energy in the calculation of the FCC-based Al-rich part of the Al-Sc phase diagram. It is found that these *vibrational contributions give rise to a factor of twenty increase in the calculated solubility limits for Sc in FCC Al*, ultimately resulting in a good level of agreement between measurements and calculated results. This work clearly demonstrates a significant effect of vibrational entropy upon first-principles calculated phase boundaries in a substitutional alloy.

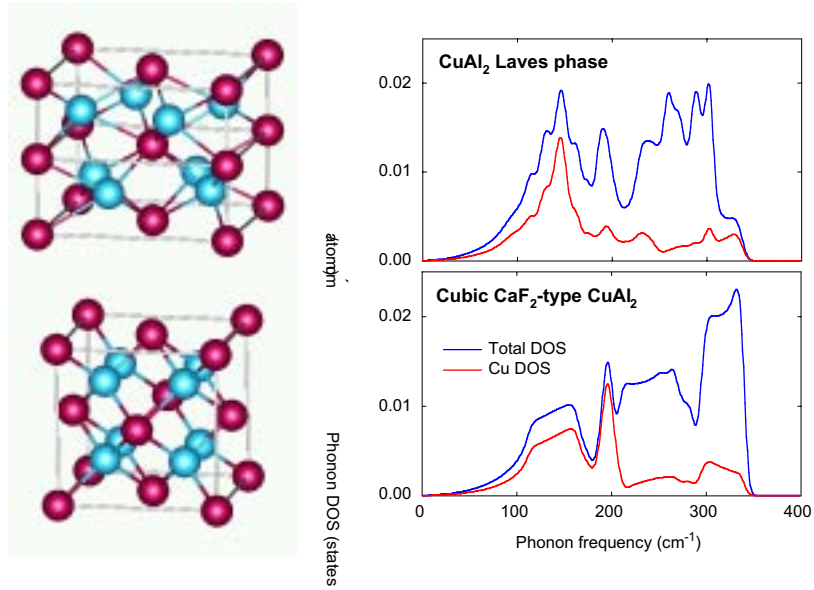


**Figure 1.** Structure of Al<sub>2</sub>Cu precipitate phases: tetragonal *C16* phase (top left) and cubic CaF<sub>2</sub>-type structure (bottom left). Al atoms are purple and Cu atoms are light blue. The calculated phonon densities of states (DOS) for both phases are shown in the right panel. Vibrational entropy of the tetragonal *C16* (Al<sub>2</sub>Cu) phase is  $\approx +0.35k_B/\text{atom}$  higher due to larger spectral weight at low frequencies, arising from low-frequency optical branches between 100 cm<sup>-1</sup> and 200 cm<sup>-1</sup>.

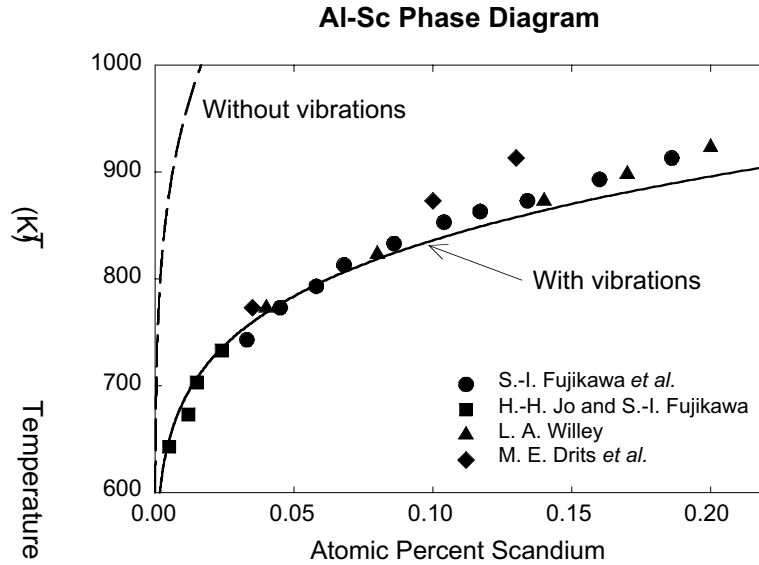


**Figure 2.** Al-rich end of the Al-Sc phase diagram. Symbols represent values for the solubility limits of Sc in FCC Al obtained from experimental resistivity measurements. Also shown are solubility limits calculated from the first-principles without (dashed line) and with (solid line) vibrational entropy contributions.

## Surface Alloys

G. E. Thayer, N. C. Bartelt, A.K. Schmid, V. Ozolins, M. Asta, J. J. Hoyt, R. Q. Hwang

### Motivation:

Surface alloys are ideal model systems for understanding alloying thermodynamics under reduced coordination and external elastic stress. Elastic effects play a particularly important role in promoting mixing tendencies and stabilizing ordered surface alloy structures in systems that do not mix in the bulk.

### Accomplishment:

For instance, we have predicted theoretically that Co and Ag (which are bulk-immiscible in both solid and liquid states) will form pseudomorphic monolayer alloys on the Ru(0001) surface. Our theoretical predictions were successfully verified experimentally at Sandia using direct atomic-scale surface-imaging techniques. These experiments found that thermally annealed ultrathin Co-Ag films on Ru(0001) exhibit a pseudomorphic  $\text{Co}_{0.6}\text{Ag}_{0.4}$  alloy phase with a disordered nanoscale “droplet” structure (see Fig. 1). This alloy phase coexists with a dislocated Ag monolayer phase. Surface alloying in Co-Ag/Ru(0001) is favored by efficient strain relief at Ag/Co interfaces (see the brightly colored Co atoms around the patches of Ag in Fig. 1), which competes with the other available mechanism of strain relief: formation of misfit dislocations in monolayer Ag film.

### Impact:

Currently, we are developing a general theoretical framework for treating long-range elastic and short-range chemical interactions on an equal footing from first-principles electronic-structure calculations. We plan to extend our models to study how surface alloys approach the thermodynamic equilibrium. The associated ordering/phase-separation kinetics is very interesting due to existence of surface diffusion mechanisms that are qualitatively different from bulk diffusion.

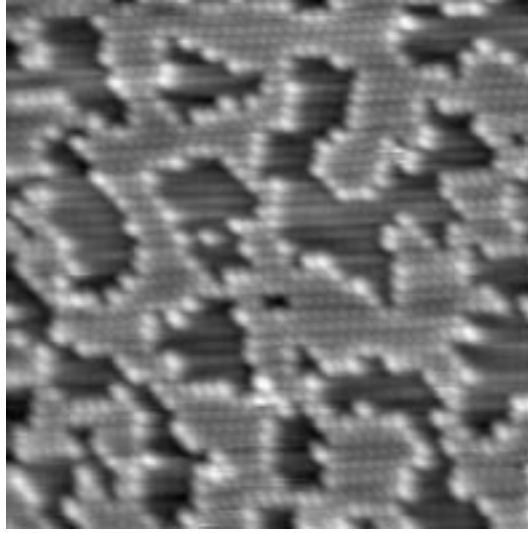


**Figure 1.** Atomic-resolution STM image of a thermally annealed Co-Ag surface alloy on Ru(0001), showing a disordered droplet structure. Ag atoms are dark and Co atoms are bright spots. Increased brightness of Co atoms near Co/Ag interfaces is due to large atomic displacements, indicative of an efficient strain relief in the alloy phase.

## Computation of the Solid-Liquid Interfacial Free Energy in Ni

JJ Hoyt, M Asta and A. Karma (Northeastern University)

### Motivation:

The microscopic solvability theory of dendritic solidification predicts that the growth velocity is extremely sensitive to the anisotropy in the solid-liquid interfacial free energy. The theory has remained largely untested due to the enormous difficulty of measuring or computing the very small anisotropies, on the order of 1% for metals. We have developed a computational method that is capable of resolving the small anisotropy of the interfacial energy.

### Accomplishment:

The interfacial energy  $\gamma$  can be written as  $\gamma_o [1 + \epsilon_4 \cos(4\theta)]$  where  $\gamma_o$  is the average energy,  $\theta$  is the angle between the surface normal and the 100 direction, the factor of 4 reflects the four fold symmetry of the crystal and  $\epsilon_4$  is the small anisotropy. A solid-liquid interface at the melting temperature will fluctuate about a planar configuration and it can be shown that the power spectrum of the interface position averaged over many configurations, ie. the quantity  $\langle |A(k)|^2 \rangle$  where  $A(k)$  is the Fourier transform of the interface height, is proportional to  $k^{-2}$ . Furthermore the constant of proportionality depends on the reciprocal of  $\gamma_o [1 \pm 15\epsilon_4]$  where the plus sign refers to fluctuations about a 110 interface and the minus sign holds when a 100 interface is considered. The factor of 15 implies that the anisotropy is significantly magnified when fluctuations are computed and hence small values of  $\epsilon_4$  can be resolved. We have performed molecular dynamics simulations of pure Ni using embedded atom potentials to illustrate the above technique. Figure 1 shows a log-log plot of the fluctuation spectra for both the 100 and 110 orientations. The solid lines in each case demonstrate that the correct  $k^{-2}$  dependence is observed. Figure 2 shows the reciprocal of the fluctuation term vs.  $k^2$  and from the slopes of these lines  $\gamma_o$  is found to be 315mJ/m<sup>2</sup>, in good agreement with empirical estimates, and the anisotropy is 1.83%.

### Significance:

The computations described above represent the first time the solid-liquid interfacial free energy and its small anisotropy have been calculated. The results pave the way for critical tests of the generally accepted microscopic solvability theory of dendrite growth. The quantities computed are also necessary input into phase field modeling of alloy solidification.

### Publications:

J. J. Hoyt, B. Sadigh, M. Asta and S. M. Foiles, "Kinetic Phase Field Parameters for the Cu-Ni System Derived from Atomistic Computations," *Acta Mater.*, **47**, 3181 (1999).

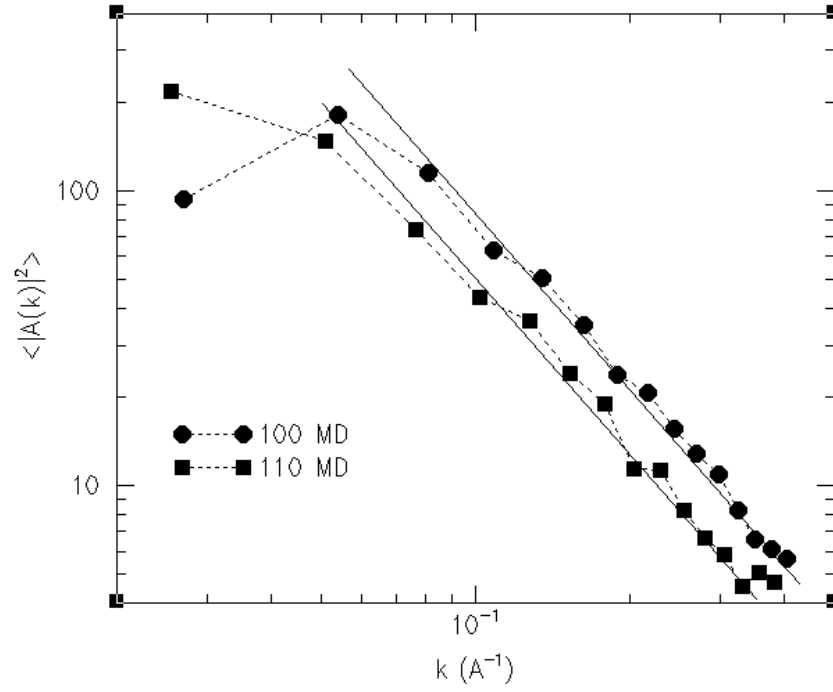


Fig. 1. Computed fluctuation spectra of the solid-liquid interface in pure Ni. The correct  $k^{-2}$  dependence is observed (solid lines) for both the 100 and 110 orientation.

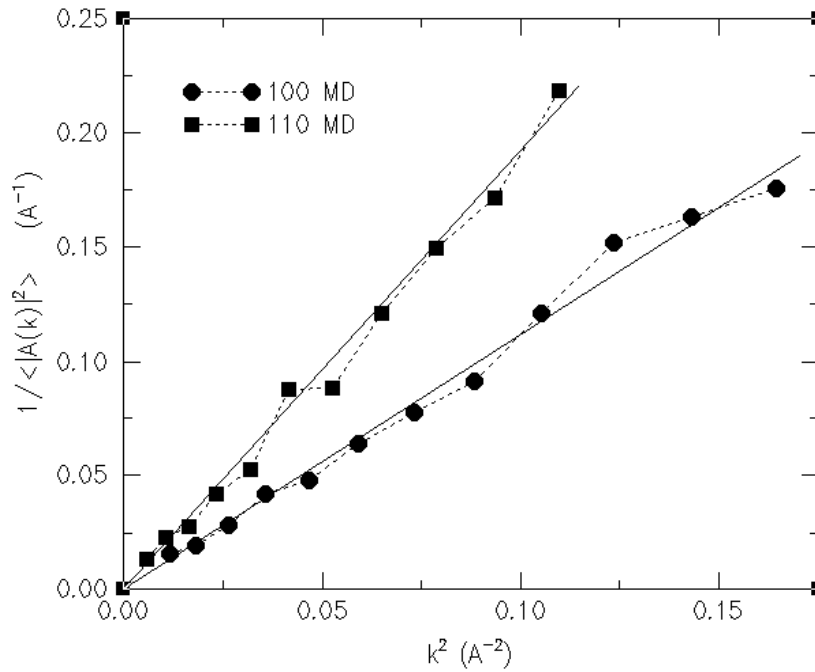


Fig. 2. Reciprocal of the average power spectrum vs.  $k^2$  for the 100 and 110 orientations in pure Ni. From the slopes of the lines a value of the interfacial free energy equal to 315 mJ/m<sup>2</sup> is found and an anisotropy factor of 1.83% is obtained.